# Experimental measurement of scattering coefficients in mesoscopic conductors

K. L. Shepard,* M. L. Roukes, and B. P. van der Gaag
*Bellcore, Red Bank, New Jersey 07701*
(Received 16 April 1992)

We describe a general experimental approach yielding the entire transmission matrix of a multiprobe mesoscopic conductor. Results are presented for several new investigations with ballistic semiconductor nanostructures enabled by this technique. We measure the transmission coefficients for an *open* cross junction employing a sample design which is an almost literal realization of the Landauer-Büttiker model and verify that these transmission coefficients are consistent with Hall and bend resistance anomalies obtained by resistance measurements at low magnetic fields. Other investigations utilize a *pinched* cross junction in which two of the probes are separated from the channel by quantum point contacts. This series arrangement of point contacts allows a sensitive momentum spectroscopy of the emitted distribution. Even in the case of a single propagating mode through the constrictions, we observe *modal features* in the outgoing distribution. This indicates that the potential is spatially nonadiabatic even though conductance quantization is observed. This *pinched* geometry also allows the first fully characterized realization of weakly coupled probes.

## I. INTRODUCTION

The Landauer-Büttiker formula,[1] which treats transport as a scattering problem,[2,3] has provided the context for understanding transport in many types of mesoscopic structures. The formula's success in describing transport in ballistic structures relies on the fact that electrical conduction is dominated by a single scattering region. In this work, we present an experimental technique enabling *measurement* of the transmission coefficients for ballistic multiprobe microstructures. We will describe samples we have designed which are almost literal realizations of the idealized Landauer-Büttiker model.

A generalized multiprobe scattering structure as microfabricated in a degenerate two-dimensional electron gas (2DEG) is shown in Fig. 1. A scattering region is fed by quasi-one-dimensional *leads*, each of which has a finite number of occupied transverse states, or *modes*. An incoming electron in mode $n$ of lead $j$ is scattered into mode $m$ of lead $i$. The quantum-mechanical amplitude for this process is given by $t_{ij,mn}$. The Landauer-Büttiker formula relates currents and voltages to these amplitudes within the context of linear response.[1] To each lead $i$ is attached a *reservoir* in a state of internal equilibrium at a chemical potential $\mu_i$. The reservoirs are assumed to contact the leads without introducing any additional sources of scattering;[4] that is, the connection between reservoir and lead is reflectionless. All voltage drops and, therefore, all dissipation occur within the reservoirs, as thermalized electrons in the reservoirs at their respective chemical potentials $\mu_i$ are injected into or collected from these leads.[5]

The Landauer-Büttiker formula at zero temperature is given by

$$\frac{h}{2e}I_i = -N_i\mu_i + \sum_j T_{ij}\mu_j, \tag{1}$$

where $i$ and $j$ are indices labeling the leads. $N_i$ is the number of propagating modes in the lead $i$; $N_i = \sum_j T_{ij}$. We use the convention that positive currents imply flow *into* the leads. The $T_{ij}$ are *transmission coefficients*, given by the transmission probabilities evaluated at the Fermi energy $E_F$ and summed over channel indices:

$$T_{ij} = \sum_{mn} |t_{ij,mn}(E_F)|^2. \tag{2}$$

These represent the total transmission (i.e., number of effective propagating modes) from all occupied modes incident upon the scattering region from lead $j$ and ultimately emerging into outgoing occupied modes of lead $i$. The Landauer-Büttiker formula follows the spirit of

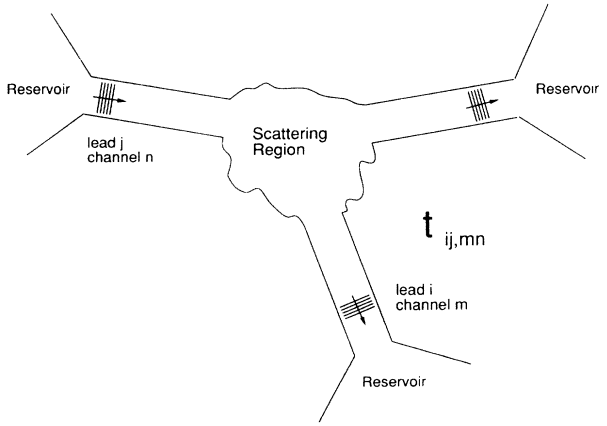


FIG. 1. Generalized scattering structure microfabricated in a 2DEG. An incoming electron in mode $m$ of lead $i$ is scattered into mode $n$ or lead $j$ with transmission amplitude $t_{ij,mn}$. Current is fed into each lead by a reservoir at chemical potential $\mu_i$.

 

the Kubo formula[6] in that transport properties in the limit of linear response[7,8] are related to the equilibrium properties of the system at the Fermi energy. Because this scattering formalism applies only in the limit of linear response, it deals exclusively with elastic scattering between occupied modes near $E_F$. Finite temperature solely plays the role of "smearing" the distribution function; the transmission coefficients are weighted by the derivative of the Fermi function:

$$T_{ij} = \sum_{mn} \int dE \left( \frac{-\partial f}{\partial E} \right) |t_{ij,mn}(E)|^2 .$$

The formalism culminates in the development of measurable voltages at each reservoir given by the steady-state chemical potentials over the electronic charge, $V_i = \mu_i / e$.

Time-reversal invariance implies that the microscopic transmission amplitudes satisfy

$$t_{ij,mn}(B) = t^*_{ji,nm}(-B). \tag{3}$$

This implies that the transmission coefficients satisfy the reciprocity relation:[1]

$$T_{ij}(B) = T_{ji}(-B). \tag{4}$$

Equations (1) and (2) are derived under the assumption of quantum-mechanical phase coherence. Büttiker, however, has shown that the introduction of phase-breaking scatterers is equivalent to the introduction of additional reservoirs, which one constrains to have no net effect on the current.[9] The Landauer-Büttiker formula and the reciprocity relations, therefore, hold equally well in the case of *classical* ballistic transport.

Equation (1) gives the conductance of the multiprobe system; that is, the current response to voltages applied to each of the leads. Thus far, only resistances have been measured experimentally. In this case, fixed currents are applied to the leads and voltages are measured. In a four-probe measurement, we apply a given current at *current* leads (into $k$ and out $l$) and measure the chemical potential difference at *voltage* leads (from $m$ to $n$) where the currents are constrained to be zero. This standard experimental configuration permits study of one portion of the total voltage drop along the current path. From Eq. (1),[1] generalized four-probe resistances are of the form

$$R_{kl,mn} = \frac{h}{2e^2} \frac{T_{mk} T_{nl} - T_{ml} T_{nk}}{D}, \tag{5}$$

where $D$ is any cofactor of the matrix defined by Eq. (1). As these $R_{kl,mn}$ are complicated functions of the transmission coefficients, they provide only indirect information about the scattering properties of the conductor. A more direct approach is desired to study the detailed behavior of the separate elements $T_{ij}$.

This paper is organized as follows. In Sec. II, we describe four-probe samples specifically designed for this experiment. In Sec. III, we discuss transmission coefficients we obtain for the *open* cross junction, which is fourfold symmetric and, therefore, has no geometrical distrinction between the probes. This geometry constitutes a "simplest case" test of the technique. In Sec. IV, we discuss experiments in a *pinched* cross junction, in which quantum point contacts are used to separate *two* of the probes from the main conductor. This facilitates two interesting experiments. First, the geometry allows a momentum spectroscopy of electrons emitted from one of the quantum point contacts. Interesting quantum effects are present in this distribution which provide details on the nature of conductance quantization. Second, we also use this configuration to study the perturbation upon the measurement caused by probes in the ballistic regime.

## II. SAMPLES AND EXPERIMENTAL DETAILS

### A. Measuring the transmission coefficients

As a starting point, we describe a simple means of measuring the transmission coefficients of a four-probe conductor. We note that conventional resistance measurements implicitly involve the imposition of boundary conditions upon the *currents* $I_i$. We fix the current to flow only between two reservoirs, which we designate as current contacts. This is achieved by their connection to an external source and sink of electrons. The other reservoirs are used to measure voltages; thus, currents through these contacts are constrained to be zero. If instead of these boundary conditions, we fix the *chemical potentials*, we obtain an immediate simplification in Eq. (1). Specifically, we source a (fixed) current $I_1$ into reservoir 1, increasing its chemical potential to some steady-state level $\mu_1$, while equalizing $\mu_i$ at the other reservoirs by an ideal short-circuit connection. We are thus free to rescale all of the equalized $\mu_i$ in the collection leads such that $\mu_2 = \mu_3 = \mu_4 \equiv 0$. Under these conditions, the currents through these short-circuit terminations are measured with ideal ammeters (see Fig. 2). Equation (1) then simplifies to the form

$$\frac{h}{2e} \begin{pmatrix} I_1 \\ -I_2 \\ -I_3 \\ -I_4 \end{pmatrix} = \begin{pmatrix} T_{11} & T_{21} & T_{31} & T_{41} \\ T_{12} & T_{22} & T_{32} & T_{42} \\ T_{13} & T_{23} & T_{33} & T_{43} \\ T_{14} & T_{24} & T_{34} & T_{44} \end{pmatrix} \begin{pmatrix} \mu_1 \\ 0 \\ 0 \\ 0 \end{pmatrix} - N_1 \begin{pmatrix} \mu_1 \\ 0 \\ 0 \\ 0 \end{pmatrix} . \tag{6}$$

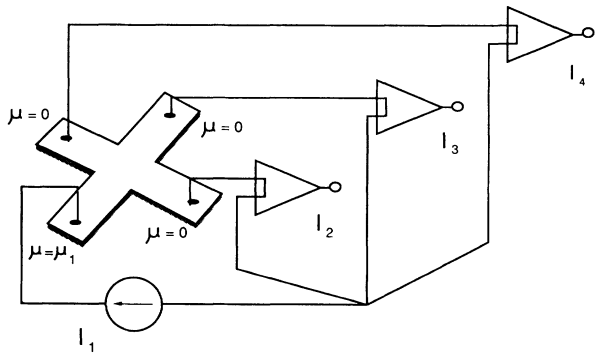


FIG. 2. Conceptual basis for the **T**-measurement technique. We source a current $I_1$ into reservoir 1, increasing its chemical potential to some level $\mu_1$, while equalizing $\mu_i$ at the other reservoirs by an ideal short-circuit connection through current preamplifiers.

One immediately obtains the first column of the transmission matrix by measurement of the currents $I_2$, $I_3$, and $I_4$. The off-diagonal $T_{ij}$ are directly proportional to the currents measured by the ammeters

$$T_{i1} = \frac{h}{2e}\frac{I_i}{\mu_1} \quad (i \neq 1) \tag{7}$$

while

$$(T_{11} - N_1) = \frac{h}{2e}\frac{I_1}{\mu_1}. \tag{8}$$

The other columns of the transmission matrix can be obtained by changing the source lead and following the same procedure.

In an experiment, however, the situation is less ideal. Real current paths used to short-circuit the reservoirs contain finite resistances such as those in the wire bonds, contacts, external leads, and current amplifiers. For each path from the reservoirs to the common external point defined as "ground," both the resistance and the current carried will be unique. The resulting path-specific potential drops which develop in steady state render external short-circuit connections ineffective at equalizing the $\mu_i$ which are *internal* to the sample.

We circumvent this difficulty by including a separate current contact ($I$ contact) and voltage contact ($V$ contact) at each reservoir. This pair of contacts enables us to simultaneously and separately monitor all the $\mu_i$ in the presence of current flow. With this configuration, one can actively null differences between the three chemical potentials of the collection reservoirs by introducing external, variable terminating impedances between each (sink) $I$ contact and "ground." This dynamic equalization of the $\mu_i$ at the current collection contacts permits the simplication of Eq. (6) to be achieved experimentally. A flow chart in Fig. 3 outlines this procedure for a four-probe device.

Applying these studies to four-probe conductors requires a self-consistent adjustment at each of three reservoirs for every value of magnetic field. In practice, we have found this technique to be more difficult than an alternative, mathematically analogous, procedure. This second approach employs *static* terminations and involves building a set of linear equations, through a set of successive measurements (sweeps) where these terminations are changed. We ultimately solve the set of linear equations to obtain the transmission matrix. This second approach to the technique is implemented as follows. Current (typically 10 nA) is injected into the current contacts of the injection reservoir and extracted and measured through current preamplifiers through the current contacts of the three collection reservoirs. The chemical potentials (voltages) of these three collection reservoirs are measured with respect to the injecting reservoir (referenced to $V = 0$). (In the work described herein, we perform our experiments at 2 K using conventional lock-in techniques at a frequency of $f = 14$ Hz.) We simultaneously obtain complete sets of separate traces for *all* the voltages and currents as a function of magnetic field for each of seven different static current terminations.

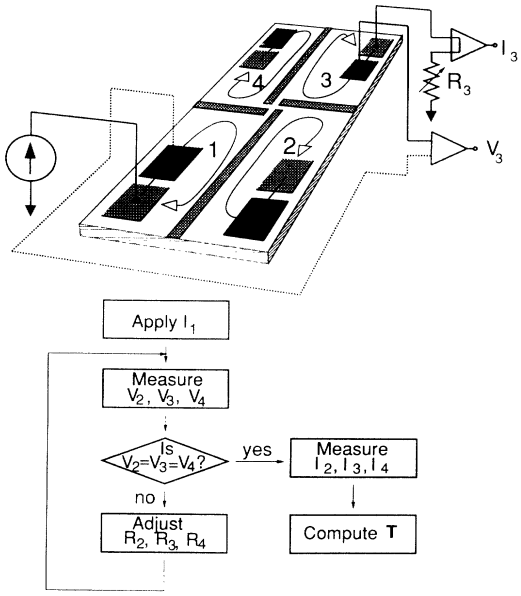


FIG. 3. One possible implementation of the **T**-measurement technique. Arrows show the direction of current flow for $B$ directed upward. Assignment of current (light shading) and voltage (dark shading) contacts depends upon field orientation. For clarity, only connection to reservoirs 1 and 3 are shown.

We have represented the terminations used for the *open cross junction* in Fig. 4 for the case of current introduced via lead 1. These represent the complete set of separate configurations by which current can be collected from one (three configurations), two (three configurations), or all three (one configuration) remaining leads.

For each magnetic-field point in the sweep, this provides an overdetermined linear system which we subsequently solve numerically to extract the transmission coefficients. Consider, for example, lead 2. For each of the seven configurations (denoted by the index $\alpha$), we obtain an equation of the form

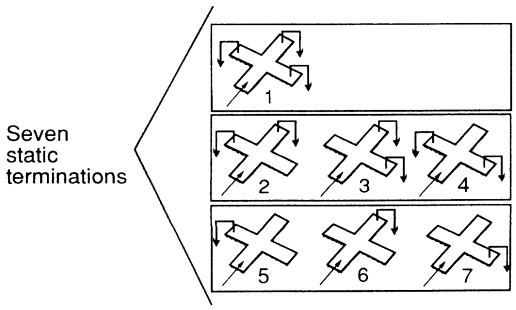


FIG. 4. Representation of the seven different static current terminations used to solve for **T** for the case of current introduced via lead 1. For the case of geometries in which there is only very small transmission through a given lead, the open circuit connection is replaced by a $\approx$ 10-k$\Omega$ shunt connecton to ground.

$$I_2^{(\alpha)} = \frac{2e}{h}(T'_{22}V_2^{(\alpha)} + T'_{23}V_3^{(\alpha)} + T'_{24}V_4^{(\alpha)}), \quad (9)$$

where $T'_{ij} = T_{ij} - N_i\delta_{ij}$. In matrix form, this complete set becomes

$$\mathbf{I}_2 = \frac{2e^2}{h}\mathbf{V}\mathbf{T}'^2, \quad (10)$$

which has dimensions

$$[7 \times 1] = [7 \times 3]\,[3 \times 1]\,. \quad (11)$$

The least-squares solution of this linear system is given by

$$\bar{\mathbf{T}}'_2 = (\mathbf{V}^T\mathbf{V})^{-1}\mathbf{V}^T\mathbf{I}_2. \quad (12)$$

This procedure can then be repeated using data which had been obtained simultaneously for leads 1, 3, and 4 and three columns of $T$ are thereby deduced. One can obtain the remaining column of $\mathbf{T}$, i.e., the $T_{i1}$'s, by injecting current into a different lead and repeating the procedure. We find, in general, that our approach provides a set of transmission coefficients satisfying the reciprocity relation of Eq. (3) to within a few percent.

Because our set of terminations $\alpha$ provides a linear system which is overdetermined, we can also extract *variances* for each transmission coefficient. We shall see that these provide additional insights into the mechanisms of scattering in these samples. Specifically, consider the linear system solved to find $T_{42}$:

$$I_4^{(\alpha)} = T_{42}V_2^{(\alpha)} + T_{43}V_3^{(\alpha)} + (T_{44} - N_4)V_4^{(\alpha)}. \quad (13)$$

We take data for seven configurations (once again denoted by the configuration index $\alpha$) to find the three coefficients, $T_{42}$, $T_{43}$, and $T_{44} - N_4$. This leaves us with four degrees of freedom. We assign all the error in the least-squares fit to an "effective" error in measuring the current $I_4$ (Ref. 10)

$$\sigma^2_{I_4} \approx \tfrac{1}{4}\sum_{i=1}^{7}(I_4^{(i)} - \bar{T}_{42}V_2^{(i)})^2. \quad (14)$$

$\bar{T}_{42}$ denotes the transmission coefficient determined by the least-squares fit. Similarly,

$$\sigma^2_{T_{42}} \approx \frac{1}{4}\sum_{i=1}^{7}\frac{(I_4^{(i)} - \bar{T}_{42}V_2^{(i)})^2}{{V_2^{(i)}}^2}. \quad (15)$$

We shall see in Sec. IV D that this variance data sheds additional light on the underlying physics of conduction in these structures.

The assignment of $I$ contacts and $V$ contacts cannot be arbitrary in the presence of a magnetic field. Consider our eight-contact, four-reservoir device pictured in Fig. 3. Arrows show the direction of current flow for a magnetic field directed upward with respect to the plane. With this field configuration, voltage probes must be in equilibrium with the electrons incoming from the current probes. This requires that current entering a current probe must first enter the voltage probe, before passing into the scattering region. The choice of contacts shown in Fig. 3 assures this for upwardly directed magnetic fields. If the opposite choice is made, a spurious Hall potential drop will result. Changing the magnetic-field orientation must, therefore, be accompanied by a change in the choice of voltage and current contacts. These conditions are a multiprobe generalization of previous measurements of two-terminal resistances in the presence of a magnetic field.[11]

The use of two contacts for each reservoir still leaves a small background resistance associated with voltage drops within the wide 2DEG rectangular regions and the "spreading" resistance associated with the coupling of these regions to the narrow gated leads of the junction. In the few-mode regime when $R_{\rm lead} \geq 3$ kΩ, they result in only a few percent systematic corrections to the measured transmission coefficients.

In four-terminal resistance measurements, it is difficult to use a lead that is only weakly coupled to the scattering region as a *voltage probe*. The chemical potential of such a "floating" reservoir is determined by ill-defined parasitic leakage paths. In this measurement, however, each reservoir is tied to the external ground through a terminating impedance at the current contact which is smaller than any parasitic ground path. As described in Sec. IV, this allows "measurement" of four-terminal resistances with weakly coupled voltage probes. For the case of geometries in which there is only very small transmission through a given lead, we replace the open circuit connection by a $\sim$ 10 kΩ shunt connection to ground. This is sufficient to differentiate it from the short circuit, 0 Ω, configuration. This allows measurement of the transmission matrix even in the presence of nearly vanishing electron flux and proves adequate to constrain the reservoirs to avoid spurious drifts in $\mu$.

### B. Sample fabrication

The devices for our transmission coefficient measurements are patterned from a conventional modulation-doped GaAs/$Al_{0.3}Ga_{0.7}As$ heterojunction. An undoped 1-$\mu$m GaAs buffer is grown by molecular-beam epitaxy on a Cr-doped semi-insulating GaAs substrate. This is followed by an undoped 150-Å $Al_{0.3}Ga_{0.7}As$ spacer layer and a 600-Å-thick $Al_{0.3}Ga_{0.7}As$ layer, doped $1.5 \times 10^{18}$ $cm^{-3}$. Growth is terminated with a 50-Å cap layer doped $2 \times 10^{18}$ $cm^{-3}$. The 2DEG density obtained from the Shubnikov–de Haas oscillations in the magnetoresistance is $n_s = 3 \times 10^{11}$ $cm^{-2}$. The impurity-limited mobility is $1.0 \times 10^6$ $cm^2/V\,sec$ which corresponds to a transport mean-free path of $l = \frac{\hbar k_F \mu}{e} \sim 9$ $\mu$m. The Fermi wavelength is $\lambda_F = (\frac{2\pi}{n_s})^{1/2} = 46$ nm.

The device geometry used in these studies is shown in the scanning electron microscope (SEM) micrographs of Fig. 5. Twelve Au/Ge/Ni/Au Ohmic contacts are defined by optical lithography and lift-off. They are subsequently annealed into the sample to contact the 2DEG. In another mask step, Cr/Au fingers are defined which converge from these contacts into what will become the central active region of the device. A final optical lithog-

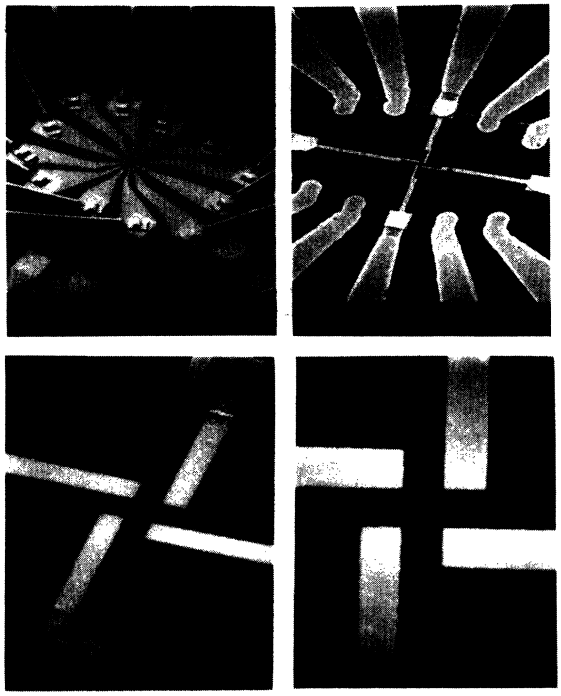

FIG. 5. SEM micrographs of one device used in this study. Top left: Wire bonds attached to twelve Au/Ge Ohmic contacts. Cr/Au fingers lead from these contacts to a central mesa. The devices are $\sim 1$ $\mu$m across. Top right: Central mesa is $20 \times 40$ $\mu$m. Four fingers are isolated from the 2DEG of the mesa by ion exposure. Four Cr-Au gates are then defined. Bottom: These gates form a central cross pattern. Adjacent gates are separated by 400 nm.

raphy step defines a central rectangular mesa $20 \times 40$ $\mu$m, which is ion-etched into the semiconductor. Two electron beam lithography steps using a JEOL JBX-5DII system follow. Using a single level PMMA mask and exposure to 500-eV $Ne^+$ ions,[12] four of the fingers are isolated from the 2DEG and the mesa is divided into four rectangular regions connected at the center. This provides a gross partitioning of the mesa into reservoirs which is effective without application of any gate bias. In a second step using a bilevel PMMA process, four Cr/Au gates, 100 nm thick, are added. When a negative bias is applied to these gates with respect to the 2DEG, the "scatterer" is defined. As an example, we show in Fig. 5 samples which allow depletion of the electron gas from beneath the gates to define an *open* cross junction.

The structures we have fabricated constitute almost literal realizations of the idealized Landauer-Büttiker model. The ion exposure separates the mesa into four rectangular regions which function as *reservoirs*. Each is designed with *two* Ohmic contacts, required for direct measurement of the transmission coefficients. Each reservior feeds a *lead*, which is formed near the center of the mesa by each adjacent pair of gates. While these gates are separated lithographically by 400 nm, depopulation measurements indicate that the actual channel produced in the 2DEG is approximately 300 nm wide at formation. The *scattering region*, which subsumes all the transport physics of the conductor, is the junction region where the leads defined by the gates connect together.

## III. TRANSPORT IN THE OPEN CROSS JUNCTION

The first structure we study is the *open* cross junction shown in Fig. 5, a "simplest case" test of the technique. The *open* cross junction has been the natural starting point for discussions of mesoscopic transport phenomena because of its $C_{4v}$ symmetry. This implies fourfold rotational symmetry and the existence of four mirror planes containing the axis of rotation. It constitutes the simplest four-probe conductor.

Two low-field magnetoresistance effects in ballistic conductors of this geometry have received considerable attention. One such effect is the suppression, or quenching, of the Hall resistance.[13] When the current is forced between opposite probes of a cross junction, a Hall resistance $R_H$ normally arises which is proportional to the transverse voltage induced between two opposite probes (see the inset of Fig. 9). $R_H$, however, is found to be suppressed near $B = 0$ in small ballistic junctions. A second effect is the negative bend resistance at $B = 0$ which decays with increasing field.[14,15] The bend resistance is proportional to the voltage drop between two adjacent probes when current is forced through the two adjacent probes on the opposite side of the junction (see the inset of Fig. 10).

The key components to the physics of transport in junctions appear to be essentially manifestations of *classical* ballistic transport.[16] Electrons introduced by the "injection" lead scatter like billiard balls from within the electrostatic sidewalls of the junction. Experiments show that this scattering can be highly specular.[17] Experiments[16] and calculations[18] suggest that short trajectories dominate the behavior of the transmission coefficients.

For an *open* cross junction with fourfold rotational symmetry, one is able to write simplified expressions for the Hall and bend resistances from Eq. (5):[18]

$$R_H = \frac{h}{2e^2}\frac{T_R^2 - T_L^2}{D}, \tag{16}$$

$$R_B = \frac{h}{2e^2}\frac{T_L T_R - T_F^2}{D}, \tag{17}$$

where $D = (T_R + T_L)[2T_F(T_F + T_R + T_L) + T_L^2 + T_R^2]$. $T_F$ $(= T_{13} = T_{24})$ is the forward transmission coefficient, $T_R$ $(= T_{21} = T_{43})$ are the right-turning coefficients, and $T_L$ $(= T_{41} = T_{23})$ are the left-turning coefficients. The magnetic-field dependencies in the transmission coefficients are manifest in the anomalous low-field magnetoresistance characteristics. The negative bend resistance near $B = 0$ is caused by the enhancement of the forward transmission over the right- and left-turning transmission coefficients in this field range. The quenching of the Hall effect may be caused by either decreasing the turning probabilities with respect to the forward trans-

mission or by decreasing the asymmetry between left- and right-turning probabilities. Various mechanism have been proposed by which these may occur.

Our technique allows us to directly measure the transmission coefficients for the first time. We are then able to determine experimentally the extent to which symmetries hold. The use of four separate gates to define the junction allows us to compensate for nonidealities such as potential variations and to obtain a confinement potential at the junction which is gate symmetric. Determining the scattering properties of the junction *experimentally* allows us to confirm the physics of measured anomalous low-field magnetoresistance characteristics through Eq. (5).

### A. Transmission coefficients

We shall display measurements of the transmission coefficients for the *open* cross junction at two different bias points: for bias $a$, $V_g = -0.7$ V; and for bias $b$, $V_g = -0.9$ V. These biases correspond to values of $E_F$ resulting in approximately five and seven occupied modes in each of the leads, respectively. In Fig. 6, we present the results for $T_F = T_{31}$, the transmission coefficient for forward propagation. The curve is peaked at $B = 0$ and falls off monotonically with increasing field as the electron distribution emitted from lead 1 is steered away from collection in lead 3.

In Figs. 7 and 8, we present the right-turning coefficients ($T_R$), $T_{41}$ and $T_{23}$, and the left-turning coefficients ($T_L$), $T_{21}$ and $T_{43}$. For magnetic fields oriented such that the Lorentz force steers the electron beam into a given lead, the turning coefficient rises to a level close to the total number of injected modes. It subsequently decreases slightly with increasing field, which we attribute to magnetic depopulation. For field values such that one would expect the electron beam to be steered *away* from collection in a given lead, we find a peak in transmission associated with specular reflection from the rounded corner of the junction. This is the first *direct* observation of such a "rebound" trajectory,[19] shown in the insets of Figs. 7 and 8. Comparing the magnitude of $T_{31}$ with the turning probabilities $T_{21}$ and $T_{41}$ near $B = 0$ confirms that forward propagation is favored. This is probably due in part to the collimation of the beam injected by lead 1, discussed in a more definitive context in Sec. IV A. We note that both $T_{21}$ and $T_{43}$ and $T_{41}$ and $T_{23}$ should be strictly equal for a junction with $C_{4v}$ symmetry. Differences arise due to the asymmetries in the actual *electrostatic* (cf. lithographic) junction potential.

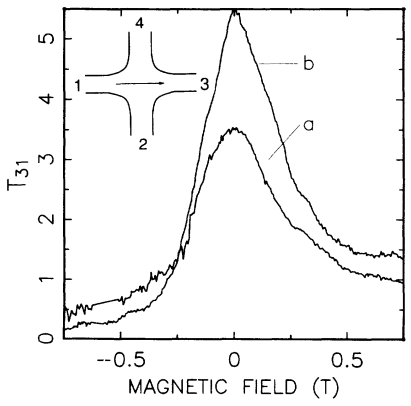


FIG. 6. Forward transmission probability $T_{31}$ for the open cross junction. We note two bias points. For bias $a$, $V_g = -0.9$ V. For bias $b$, $V_g = -0.7$ V. Inset: Ballistic trajectory at zero field.

### B. Hall and bend resistances

We use the measured transmission coefficients to calculate, or "reconstitute," the Hall and bend resistance through Eq. (5) and then compare them with direct measurements of four-terminal resistances in Figs. 9 and 10. Small discrepancies between the "reconstituted" and measured values arise because the gate bias defining the junction potential must be brought to zero and reapplied between the transmission coefficient experiment and the four-terminal resistance measurement. Changes to the

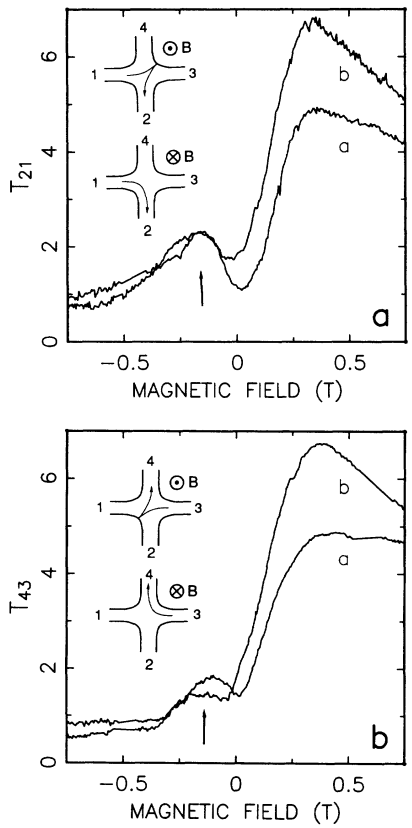


FIG. 7. Right-turning transmission probabilities for the open cross junction at biases $a$ and $b$. Arrows show field regions at which rebound trajectories occur. (a) $T_{21}$ vs magnetic field. Top inset: Ballistic trajectory showing "rebound" into lead 2. Bottom inset: Ballistic trajectory for direct steering into lead 2. (b) $T_{43}$ vs magnetic field. Top inset: Ballistic trajectory showing "rebound" into lead 4. Bottom inset: Ballistic trajectory for direct steering into lead 4.

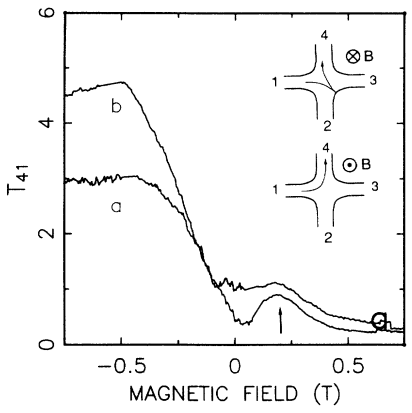


FIG. 8. Left-turning transmission probabilities for the open cross junction at biases $a$ and $b$. Arrows show field regions at which rebound trajectories occur. (a) $T_{41}$ vs magnetic field. Top inset: Ballistic trajectory showing "rebound" into lead 4. Bottom inset: Ballistic trajectory for direct steering into lead 2.

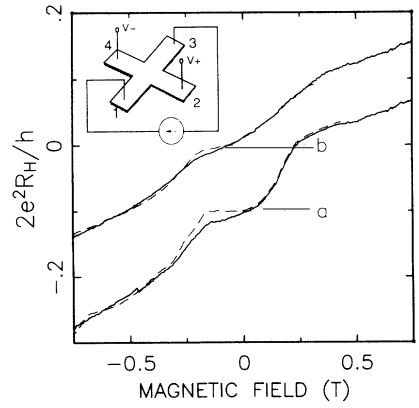


FIG. 9. Hall resistance $R_H = R_{13,24}(B)$ for the open cross junction at biases $a$ and $b$ reconstituted from the measured $T_{ij}$ (solid curves). Also shown is $R_H$, measured conventionally at each bias (dashed curves). The curve for $a$ is offset $-0.1$. Inset: Choice of current and voltage probes for this measurement.

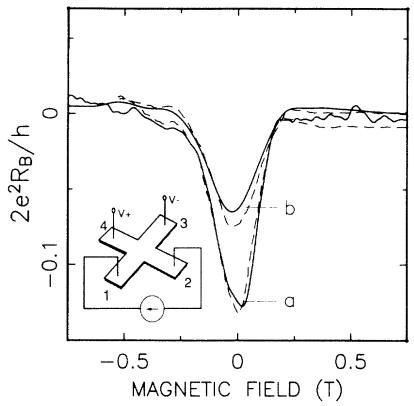


FIG. 10. Bend resistance $R_B^{(1)} = R_{12,43}(B)$ for the open cross junction at biases $a$ and $b$ reconstituted from the measured $T_{ij}$ (solid curves). Also shown is $R_B$, measured conventionally at each bias (dashed curves). Inset: Choice of current and voltage probes for this measurement.

transmission coefficients always result from this procedure, reflecting the difficulty in reachieving precisely the same confinement potential. We speculate that this occurs because of slight rearrangement of the lateral distribution of ionized donors in the donor layer.

## IV. TRANSPORT IN THE PINCHED CROSS JUNCTION

In this section, we discuss experiments in a *pinched* cross junction, in which quantum point contacts are used to separate *two* of the probes from the main conductor. We shall demonstrate that this facilitates two interesting experiments. First, this geometry allows a momentum spectroscopy of electrons emitted from a quantum point contact. Second, we use this configuration to study the perturbations upon the measurement caused by probes in the ballistic regime.

Recent work views the quantum point contact as having the form of a saddle-point potential.[20] Conductance is quantized because the potential in the constriction is locally adiabatic,[21] implying that the mode number for the transverse motion is conserved. Each mode that is successfully transmitted contributes one unit of $2e^2/h$ to the conductance. Away from the constriction, the potential necessarily becomes nonadiabatic since it ultimately widens rather abruptly to join the 2DEG. Despite intermode scattering in this region, the probability of backscatter is small and the conductance remains quantized.[28] In Sec. IV C, we will present significant modifications to the adiabatic saddle-point picture of the quantum point contact.

The "scatterer" studied in this section, the *pinched* cross junction, is shown in the SEM micrographs of Fig. 11.[22] Leads of a cross junction are, as in the *open* cross case, defined by gates separated by 400 nm. However, in this case, two of these leads are pinched by 150-nm side constrictions formed between two 50-nm-wide gate fingers. By contrast with the open cross junction, the

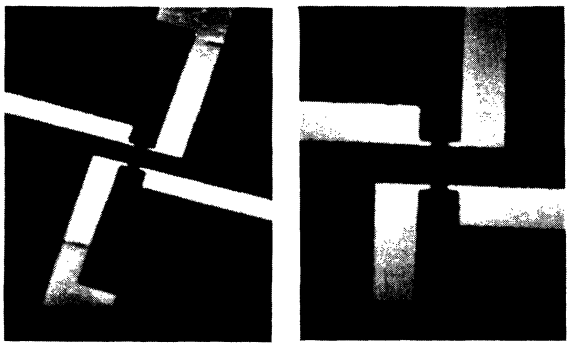

FIG. 11. SEM micrographs of the pinched cross junction. Leads of a cross junction are, as in the case of the open cross junction, defined by gates separated by 400 nm. Here, however, two of these leads are pinched by 150-nm side constrictions formed between two 50-nm-wide gate fingers.

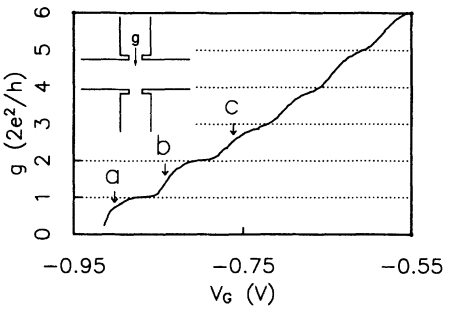


FIG. 12. Two-terminal conductance across the constrictions as a function of gate bias. Three bias ponts are labeled $a$, $b$, and $c$.

ideal pinched cross junction has only $C_{2v}$ symmetry, that is twofold rotational symmetry with two mirror planes containing the axis of rotation. In this case, the Hall and bend resistances are given by

$$R_H = \frac{h}{2e^2}\frac{T_R\tilde{T}_R - T_L\tilde{T}_L}{D}, \tag{18}$$

$$R_B^{(1)} = \frac{h}{2e^2}\frac{T_R\tilde{T}_L - T_F\tilde{T}_F}{D}, \tag{19}$$

$$R_B^{(2)} = \frac{h}{2e^2}\frac{\tilde{T}_R T_L - T_F\tilde{T}_F}{D}. \tag{20}$$

There are two distinct bend resistances in this case. $T_{R\ (L)}$ is the turning coefficient for transport from the main channel right (left) into one of the point contacts. $\tilde{T}_{R\ (L)}$ is the turning coefficient for transport from the quantum point contact right (left) into the main channel. $T_F$ is the transmission coefficient from point contact to point contact. $\tilde{T}_F$ is the transmission coefficient down the main channel.

In Fig. 12, we display the two-terminal conductance across the constrictions as a function of gate bias. The conductance is approximately quantized in units of $2e^2/h$.[23,24] We denote three bias points, labeled $a$, $b$, and $c$. These biases permit only small transmission through the constriction $t \sim 0.5, 1.5$, and 2.5, respectively, while allowing much larger transmission along the main conductor, $T \sim 7$, 8, and 10. The properties of the effective potential in the scattering region at these biases is summarized in Table I. $n_s$ is the effective two-dimensional electron gas density in the main channel, obtained from the quantum Hall effect. $L$ is the distance between the constrictions, extracted assuming hard-wall potentials from the conductance of the leads ($W = \frac{h\pi}{2e^2}\frac{g}{k_F}$). The other parameters displayed in Table I are introduced below.

### A. Forward transmission coefficient and analysis

Molenkamp *et al.*[25] measured the bend resistance with a series arrangement of point contacts to demonstrate collimation of an electron beam emitted by such a contact. Collimation refers to an electron distribution that is more peaked in the forward direction than a simple $\cos\theta$ distribution.[26] This is an effect arising from the invariance of $p_y W$ (or in the few-mode case, by the conservation of transverse mode index) in a slowly widening orifice. In a gradually tapered opening, the increasing width lowers the transverse momentum, thereby increasing the forward momentum.

Our experiments here allow forward transmission measurements even in the case of nearly vanishing electron flux. With weakly coupled reservoirs where bend resistance measurements are precluded, this permits us to explore the details of the injected momentum distribution for the first time in the few-mode quantum limit. In Fig. 13, we plot $T_{42}$ as a function of field. The curves are

TABLE I. Parameters for the pinched junction. $V_g$ is the applied negative gate bias. $n_s$ is the effective two-dimensional electron gas density in the main channel. $L$ is the distance between the constrictions, extracted from the conductance of the leads, assuming hard-wall potentials. $X^+$ ($X^-$) is the distance of the left (right) reflection point from the center of the collector. $W_c$ is the effective width of the collector.

| Bias point | $V_g$ (V) | $n_s$ (cm$^{-2}$) | $L$ (nm) | $X^+$ (nm) | $X^-$ (nm) | $W_c$ (nm) |
|---|---|---|---|---|---|---|
| $a$ | −0.9 | $1.8 \times 10^{11}$ | 210 | 55.0 | 50.0 | 28 |
| $b$ | −0.84 | $2.0 \times 10^{11}$ | 220 | 64.5 | 57.5 | 90 |
| $c$ | −0.7 | $2.2 \times 10^{11}$ | 270 | 115.0 | 83.0 | 146 |

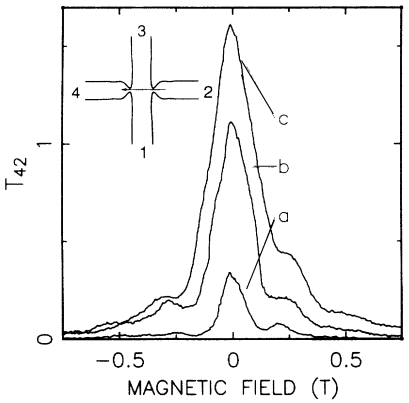


FIG. 13. Forward transmission coefficient $T_{42}$ for electrons propagating through both constrictions. Inset: Ballistic trajector at zero field.

sharply peaked near $B = 0$ but show shoulder features for fields $|B| \sim 0.3$ T which were not observed in Figure 6 for the case of the open cross junction.

The starting point for our analysis is the assumption that propagation between the two point contacts can be treated classically. The approach is similar to previous work on classical electron focusing.[27] For each point contact, we introduce a quantity $dT/d\theta$ (Ref. 29) which is the transmission per unit angle of emission. The total transmission through the point contact is then given by $T = \int_{-\pi/2}^{\pi/2} \frac{dT}{d\theta}\, d\theta$ which defines its conductance $g = \frac{2e^2}{h}T$ for spin degeneracy. The emitted electron flux per unit angle is given by $\frac{\hbar k_F}{m^*}\frac{dT}{d\theta}$. Reciprocity of the injector and collector requires that $dT/d\theta$ also define the maximal collection per unit angle.

The differential transmission per unit angle emitted by the injector (collector) at angle $\theta$ is given by $dT_{i(c)}(\theta)/d\theta$. We assume that the collector and injector have the same width, $W_c$. The maximum amount of transmission that is collected by a differential element $dx_c$ of the collector is given by

$$\left|\frac{d\theta'}{dx_c}\right| \frac{dT_c(\theta')}{d\theta'} dx_c. \tag{21}$$

$\theta'$ is the angle of collection. $x_c$ is the coordinate along the collector. For the case of point injection and point collection ($W_c/L \ll 1$),

$$T_F = \frac{W_c}{L}\frac{dT(\theta)}{d\theta}, \tag{22}$$

where

$$\frac{dT}{d\theta} = \min\left(\frac{dT_i(\theta)}{d\theta}, \frac{dT_c(\theta)}{d\theta}\right) \tag{23}$$

and $\theta$ is determined by $L/2 = r_c \sin\theta$. $r_c = (h/eB)\sqrt{n_s/2\pi}$ is the cyclotron radius and $L$ is the distance between the constrictions.

The "minimum of" result is exactly that obtained previously for the case of magnetotransport between two point contacts in series.[30] The quantized ballistic conductance of one point contact is $g_1 = \frac{2e^2}{h}N_1$ while the other is $g_2 = \frac{2e^2}{h}N_2$. In the case where transport from one point contact to the other is adiabatic (i.e., inter-Landau-level scattering is suppressed) $g_{\text{series}} = \frac{2e^2}{h}\min(N_1, N_2)$. In our case, transport is "adiabatic" if the electrons are essentially ballistic, meaning that scattering involves only small-angle events. At 2 K, acoustic phonon and electron-electron scattering are the dominant phase-breaking mechanisms. Both are small-angle scattering events, which essentially preserve forward momentum.

Using the data from Fig. 13, we use Eqs. (22) and (23) and the values for $W_c$ noted in Table I to obtain the plot of $\frac{dT}{d\theta}$ shown in Fig. 14. The assumption of point injection and collection is less valid for bias $c$ where $W_c/L \sim 0.54$ than bias $a$ where $W_c/L \sim 0.13$. We have "imaged" an injected electron beam that is more sharply peaked in the forward direction that a simple $\cos\theta$ distribution. This collimated beam has distinct side-lobe features which are present even for less than one propagating mode.

One might expect to observe corresponding features to those observed in $T_{42}$ in a straightforward four-probe measurement of the bend resistance, $R_B^{(1)}(B) = R_{12,43}(B)$ or $R_B^{(2)}(B) = R_{23,14}(B)$. In Fig. 15, we show $R_B^{(1)}(B)$ reconstituted from the measured $T_{ij}$. Also shown is $R_B^{(1)}$ measured conventionally at bias $c$. Only in this least-pinched off case can we actually obtain $R_B$ through a conventional four-probe measurement. Complications arising from use of weakly coupled probes preclude such measurements for biases $a$ and $b$; instead, we settle for reconstituted traces. Except for the central dip in $R_B$, additional corresponding features between $T_F$ and $R_B$ are almost completely absent in the measured resistance for bias $c$. In the reconstituted resistances for biases $a$ and $b$, some of the side-lobe structure in $T_{42}$ appears to be reflected in corresponding structure in $R_B$. However, in these cases the correlation is not conclusive because $R_B$ is also a function involving other transmission coefficients [cf. Eqs. (19) and (20)].

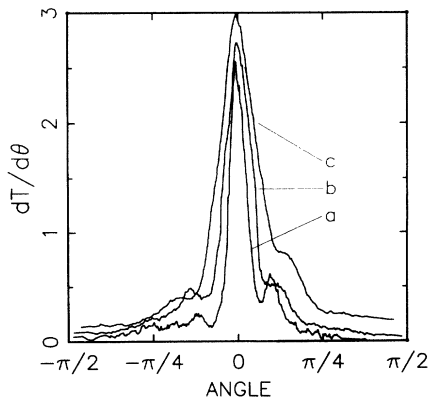


FIG. 14. $dT/d\theta$, extracted from a semiclassical analysis of the data in Fig. 13 [see Eq. (22)]. Parameters for this conversion are shown in Table I.

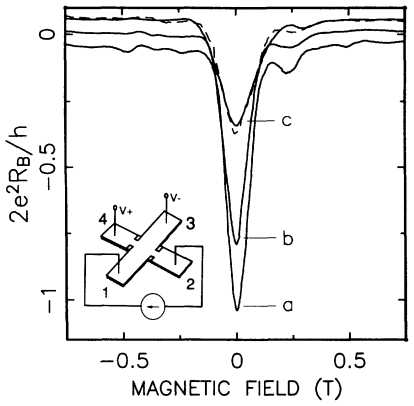


FIG. 15. Bend resistance, $R_B = R_{12,43}(B)$, for the pinched cross junction at biases $a$, $b$, and $c$ reconstituted from the measured $T_{ij}$ (solid curves). Also shown is $R_B$ measured conventionally at bias $c$ (dashed curves). Curves for $a$ and $c$ are offset by 0.05 and −0.05, respectively. Inset: Choice of current and voltage probes for this measurement.

### B. Turning coefficients

In Fig. 16, we display the right-turning coefficients ($T_R$) for transport from the main channel into one of the quantum point contacts, $T_{41}$ and $T_{23}$. In Fig. 17, we display the left-turning coefficients ($T_L$) for transport from the main channel into the other quantum point contact, $T_{21}$ and $T_{43}$. Both $T_{41}$ and $T_{23}$ and $T_{21}$ and $T_{43}$ should be strictly equal in the case of perfect $C_{2v}$ symmetry. As in the open cross case, differences arise due to the actual asymmetries of the junction potential. For magnetic fields oriented such that the Lorentz force steers the electron beam into a given lead, the transmission coefficient rises to the total number of injected modes. For field values such that we would expect the electron beam to be steered *away* from collection in a given lead, we find a peak in transmission similar to that observed in the open cross junction (cf. Figs. 7 and 8). As in the case of the open cross junction, this is due to a trajectory in which the electron beam is reflected specularly from a small segment of the smooth electrostatic boundary near the constriction and directed into the "wrong" lead as shown in the insets. In the case of bias $a$, the "rebound" peak becomes comparable in magnitude to the fully deflected flux.

Measurement of the momentum distribution of electrons emitted by the point contact, analogous to that achieved via $T_F$, is also possible using the turning coefficients $T_R$ and $T_L$. For this analysis, we use the coeffi-

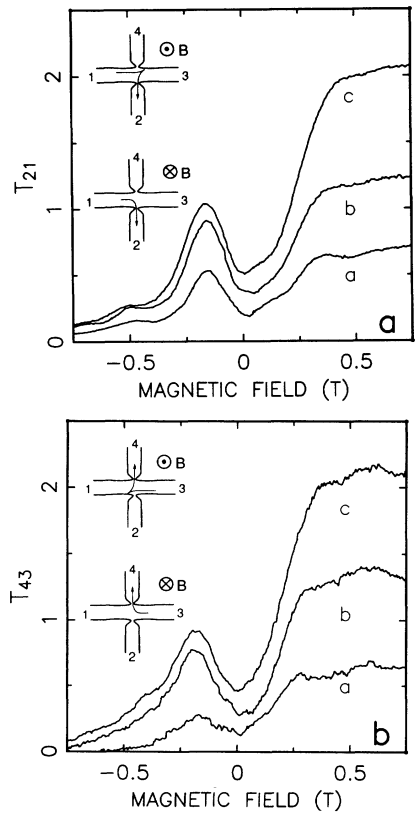


FIG. 16. Right-turning transmission probabilities for the pinched cross junction at biases $a$, $b$, and $c$. (a) $T_{21}$ vs magnetic field. Top inset: Ballistic trajectory showing "rebound" into lead 2. Bottom inset: Ballistic trajectory for direct steering into lead 2. (b) $T_{43}$ vs magnetic field. Top inset: Ballistic trajectory showing "rebound" into lead 4. Bottom inset: Ballistic trajectory for direct steering into lead 4.

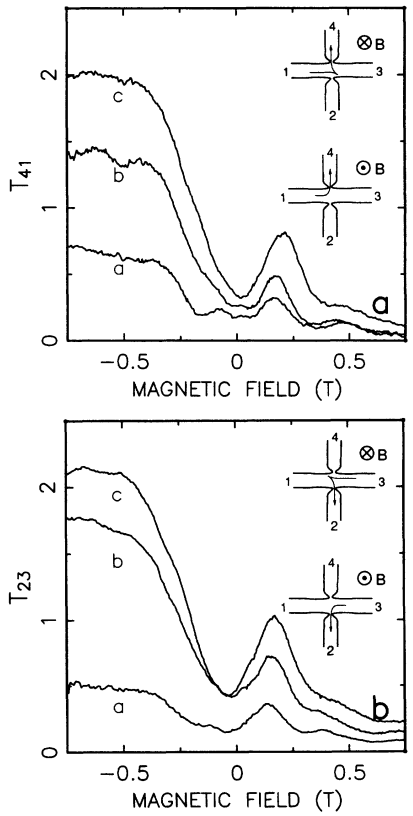


FIG. 17. Left-turning transmission probabilities for the pinched cross junction at biases $a$, $b$, and $c$. (a) $T_{41}$ vs magnetic field. Top inset: Ballistic trajectory showing "rebound" into lead 4. Bottom inset: Ballistic trajectory for direct steering into lead 4. (b) $T_{23}$ vs magnetic field. Top inset: Ballistic trajectory showing "rebound" into lead 2. Bottom inset: Ballistic trajectory for direct steering into lead 2.

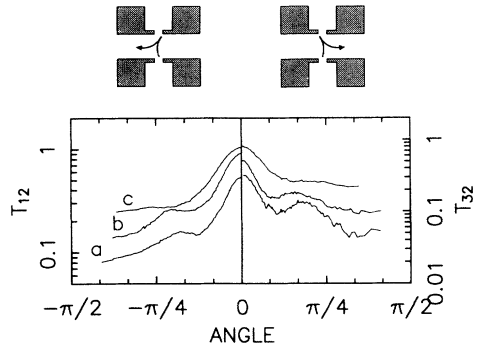


FIG. 18. Imaging with $T_{12}$ and $T_{32}$. "Rebound" portions of $T_{12}$ and $T_{32}$ plotted vs angle of emission. Top: Corresponding simple classical electron trajectories

cients for transmission from the quantum point contacts into the main channel at lead 2, $\tilde{T}_R(B) = T_L(-B) = T_{12}(B)$ and $\tilde{T}_L(B) = T_R(-B) = T_{32}(B)$. In this case, a small segment of the rounded electrostatic contours near the constriction at lead 4, directly opposite from the injector at lead 2, specularly reflects electron flux into the side probe. This is depicted in the diagrams at the top of Fig. 18. As the beam is swept past this reflecting spot, the angular profile of one half of the beam is imaged (i.e., scattered into the opposite side probe). Changing the sign of the magnetic field causes the other half of the angular profile to appear in the other side probe. In this case, a different reflecting boundary is involved, so small differences in the results for $\pm B$ are to be expected. In Fig. 18, we have plotted these "rebound" features as a function of angle of emission, $\theta$, from point contact 2. A trajectory analysis discussed in Appendix A yields the function $\theta(X^+, r_c)$, which is used to convert field into angle. Imaging via the turning coefficients involves an additional parameter, $X^+$ ($X^-$), which is the distance of the left (right) reflection point from the center of the collector point contact. Values of $X^+$ and $X^-$ used to obtain the curves of Fig. 18 are noted in Table I. They are determined by fitting the main "rebound" peaks to a zero angle of emission. We note that the curves of Fig. 18 show the same side-lobe features observed in Fig. 14. The presence of the same fine structure in $T_R$ and $T_L$ as observed in $\tilde{T}_R$ and $\tilde{T}_L$ follows from reciprocity and is due to the angular dependence of *collection* in the former case rather than of *injection* in the latter case. A consistent picture emerges, despite the fact that quantitative comparisons are rather difficult because of the complexity of the collection within the "rebound" geometry and that our hard-wall approximations only qualitatively represents the true, more rounded, potential contours.

### C. Details of calculating $dT/d\theta$

In Fig. 14, we have presented curves showing the shape of the momentum distribution ($dT/d\theta$) injected by the quantum point contact. Although propagation within the junction is essentially classical, transport at the quantum point contacts is *not*. We constrict them to the point where, at most, only a few modes propagate. In this quantum-mechanical regime, side lobes appear in the emerging beam. Let us first consider whether these side-lobe features may be attributed to secondary diffraction maxima.

For a single mode of propagation, we can achieve a collimated central beam with the *adiabatic* potential shown in the inset of Fig. 19. We calculate the injected distribution function for a wire in which only a single mode propagates at the Fermi level and which widens and then empties into a wide 2DEG region. Our calculations are performed using a recursive Green's-function technique[31,18] as discussed in Appendix B. Here, the transverse confinement potential satisfies the condition for spatial adiabaticity, given by

$$dW/dx < \frac{1}{N(x)}, \tag{24}$$

where $N(x) \approx k_F W(x)/\pi$ and $W(x)$ is the (transverse) width at (longitudinal) position $x$.[28] The resulting injected distribution in this case is shown in Fig. 19. Secondary diffraction maxima are evident at $\theta = 40°$ and $\theta = 65°$ but are orders of magnitude below the central maximum at $\theta = 0$. To compare these results with experiment, we plot $T_{42}$ in polar form, employing a logarithmic radial coordinate, in Fig. 20. Comparing with Fig. 19, it is immediately evident that diffraction *cannot* explain the side-lobe features observed in the experimentally imaged distribution, which are less than an order of magnitude smaller than the central maximum.

On the other hand, features of this magnitude can result from injection of a *multimode* distribution into a semi-infinite (2D) region. Allowed momenta for electrons in such a wire which empty into a wide 2DEG region appear as allowed points on the $k$-space semicircle $|\mathbf{k}| = k_F$ in Figs. 21(b) and 21(c). Thus, a wire injects modal features at specific angles into a 2D region.

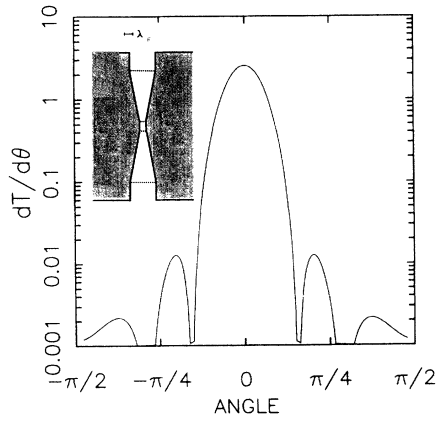


FIG. 19. $dT/d\theta$ for an *adiabatic* constriction with a single propagating mode. The center of the constriction is defined by a potential of height $0.38E_F$ and width $0.95\lambda_F$. The width and potential are graded to $3.2\lambda_F$ and zero, respectively, over a distance of greater than $9\lambda_F$. Inset: Adiabatic point contact potential for the calculation.

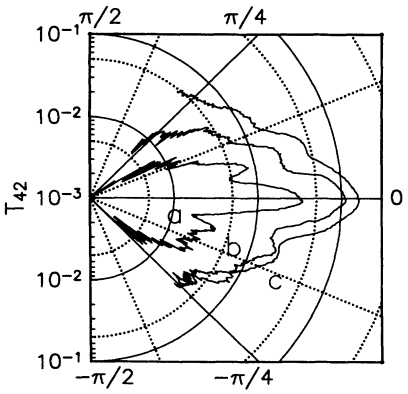


FIG. 20. $T_{42}$ as a function of angle of emission at biases $a$, $b$, and $c$. The side lobes are less than an order of magnitude down from the central peak.

Our data, however, show side lobes even for bias $a$, i.e., *even when only the lowest transverse mode propagates through the constriction.* In this case, higher modal components can only become occupied for a point contact potential which is *non-adiabatic*, as in the case of the model potential in Fig. 21(d). Here we have introduced a model potential in which a narrow saddle point (region I) defines the conductance. The potential violates the condition of Eq. (24) and is nonadiabatically graded (through region II) into a wider transition region (region III) which then empties into the wide 2DEG. In both regions I and III, momenta in the transverse direction are quantized in units of $\pi/W$. In the case of region III, each mode produces a feature in the emitted distribution centered at

$$\theta_{\pm}^{(n)} = \pm \sin^{-1}\left(\frac{n\pi}{k_F W_{\mathrm{III}}}\right). \tag{25}$$

The angular spread produced by each transverse mode is determined by diffraction. The details of the scattering potential determine the amount of flux from each occupied mode of region I which is ultimately transferred into the occupied modes of region III. In general, not all of the electrons in a given mode will be scattered to other modes. For those electrons which remain in the *same* mode as they pass from region I into region III, the increased width of III lowers their transverse momentum, $k_{\parallel}^{(n)}$, increasing their forward momentum,

$$k_{\parallel}^{(n)} = \sqrt{k_F^2 - k_{\perp}^{(n)^2}}, \tag{26}$$

and thereby collimating the emerging distribution.

Calculations by Nixon, Davies, and Baranger[32] indicate that large potential fluctuations for quantum constrictions defined on GaAs/$Al_xGa_{1-x}As$ modulation-doped 2DEG heterostructures are to be expected. These fluctuations appear to result from the random positions of the ionized donors within the doped $Al_{0.3}Ga_{0.7}As$ layer.[33] Potential variations which are large fractions of the Fermi energy can occur on length scales comparable with the Fermi wavelength. Near the edges of the constriction where the potential rises to meet the Fermi energy, these fluctuations are most pronounced. Thus, the depletion region defining the effective boundaries of the constriction (shaded) will not follow the smooth contours of the gates themselves. In a *short* ballistic constriction, we expect that this will *in general* result in a conduc-

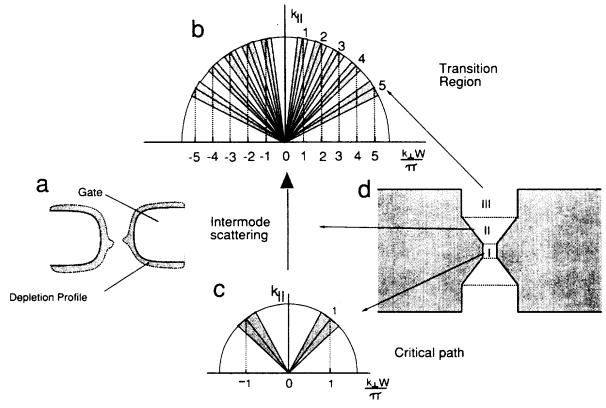


FIG. 21. Critical path model of a quantum point contact. (a) The depletion region defining the *effective* boundaries of the constriction (shaded) do not follow the smooth contour of the gates themselves. (b) Momenta on the $|\mathbf{k}| = k_F$ shell that would be emitted from region III. (c) Momenta on the $|\mathbf{k}| = k_F$ shell that would be emitted from region I. (d) Nonadiabatic model potential. The narrowest region (I) of width $W_{\mathrm{I}}$ and potential $V_{\mathrm{I}}$ empties into the transition region (III) or width $W_{\mathrm{III}}$ and length $L_{\mathrm{III}}$. These are connected by a nonadiabatic region (II), of length $L_{\mathrm{II}}$, with width and potential both linearly graded to match at regions I and III.

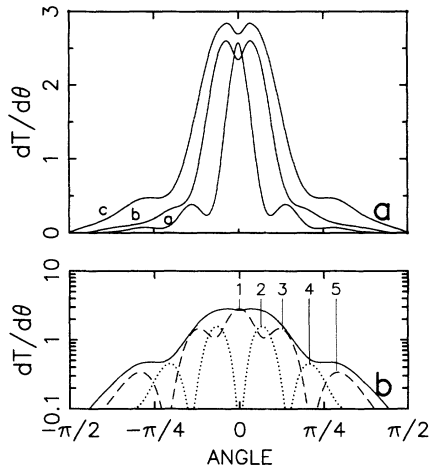


FIG. 22. (a) $dT/d\theta$ for the *nonadiabatic* point contact potential of Fig. 19 with $L_{\mathrm{II}} = 0.8\lambda_F$, $W_{\mathrm{III}} = 3.2\lambda_F$, and $L_{\mathrm{III}} = 1.6\lambda_F$. Curves $a$, $b$, and $c$ correspond to 1, 2, and 3 injected modes, respectively. For curve $a$, $b$, and $c$, $W_{\mathrm{I}} = 0.95$, 1.3, and $1.6\lambda_F$, respectively; while $V_I = 0.38$, 0.04, and $0.00E_F$, respectively. (Cf. the experimental results of Fig. 14.) (b) Modal decomposition of curve $c$ into even (dotted) and odd (dashed) components. Calculated angular peak positions for transverse modes 1 through 5 of region III are labeled.

tance controlled by a *single*, low density, narrow region — a critical path.

The model potential of Fig. 21(d) simulates this situation. We now use this potential in additional calculations. The narrow region (I) of width $W_I$, potential $V_I$, and length $L_I = 1.6\lambda_F$ empties into the transition region (III) of fixed width $W_{III} = 3.2\lambda_F$, length $L_{III} = 1.6\lambda_F$, and potential $V_{III} = 0$. The nonadiabatic region (II) has fixed length, $L_{II} = 1.6\lambda_F$, with width and potential both linearly graded to match at regions I and II. In Fig. 22(a), we plot the calculated flux distribution $dT/d\theta$ for one, two, and three modes of propagation through the saddle point (labeled *a*, *b*, and *c*, respectively). For curves *a*, *b*, and *c*, $W_I = 0.95, 1.3$, and $1.6\lambda_F$, while $V_I = 0.38, 0.04$, and $0.00E_F$, respectively. We can compare these calculations with the experimental results for $dT/d\theta$ in Fig. 14 and see strong qualitative agreement. In the calculated results of Fig. 22(b), we show the modal decomposition of curve *c* into even- and odd-parity components. In our idealized model, these are separately conserved because of the mirror-plane symmetry of the potential of Fig. 21(d). Calculated angular peak positions for transverse modes 1 through 5 of region III are labeled. For curve *c* of Fig. 22(a), the predominant "shoulders" of the sum curve arise from intermode scattering into the fourth and fifth modes. For curve *a*, however, we find that analogous "shoulders" arise *solely* due to scattering from mode 1 into mode 3.

In additional calculations presented in Fig. 23, we show the importance of the transition region (region III). We employ a potential and Fermi energy which result in a single mode of propagation through the saddle point ($V_I = 0.38E_F$, $W_I = 0.95\lambda_F$). The length of the transition region is progressively decreased from $2.4\lambda_F$ to 0, while the length of the nonadiabatic region is held at fixed length, $L_{II} = 1.6\lambda_F$. As $W_{III}$ is reduced, we find that diffraction boadens the angular spread of the modal features of $dT/d\theta$ until they coalesce and are lost in a single broad peak.

Finally, we show the importance of the nonadiabatic

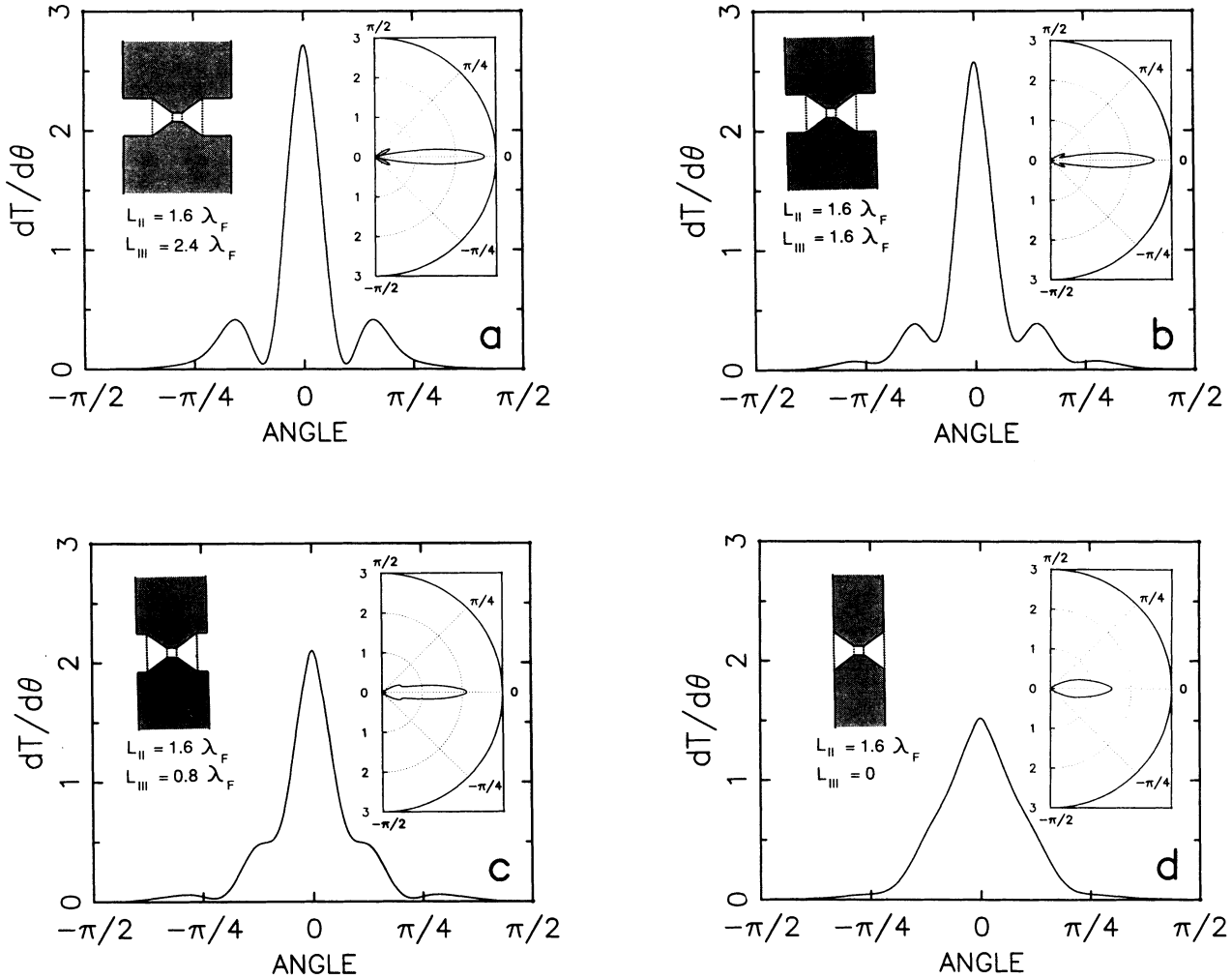


FIG. 23. Importance of the transition region. $dT/d\theta$ for the case of a single mode propagating through the saddle point ($W_I = 0.95\lambda_F$, $V_I = 0.38E_F$). The nonadiabatic region is of fixed length $L_{II} = 1.6\lambda_F$. Right inset of each plot is a corresponding polar representation. Left inset of each plot is a representation of the model potential. $W_{III}$ is successively reduced. (a) $W_{III} = 2.4\lambda_F$, (b) $W_{III} = 1.6\lambda_F$, (c) $W_{III} = 0.8\lambda_F$, (d) $W_{III} = 0$.

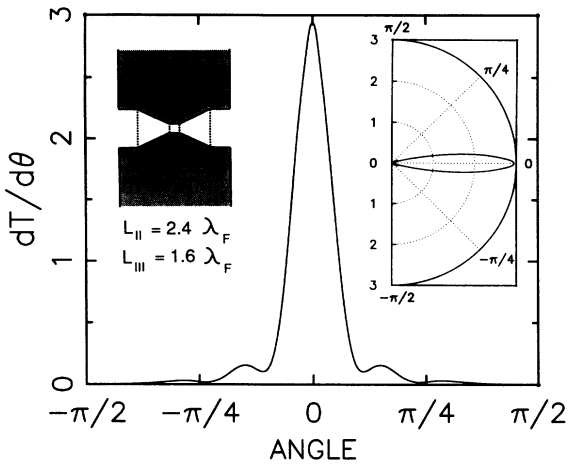


FIG. 24. Importance of the nonadiabatic regon. $dT/d\theta$ for the case of a single mode propagating through the saddle point ($W_I = 0.95\lambda_F$, $V_I = 0.38E_F$ ) [cf. Fig. 23(b)]. In this case, $L_{II} = 2.4\lambda_F$, $L_{III} = 1.6\lambda_F$. Increasing the length of region II decreases intermode scattering. Right inset: Corresponding polar representation. Left inset: Representation of the model potential.

region in mode conversion. We focus on the mode conversion from the first to the third modes, which is manifested as the shoulder as the shoulder in the emitted flux distribution for curve *a* of Fig. 22(a). Increasing the length of region II while holding other parameters fixed acts to decrease the amount of nonadiabaticity within the model potential [Eq. (24)]. In Fig. 24, we plot $dT/d\theta$ for the nonadiabatic region lengthened from $L_{II} = 0.8\lambda_F$ to $L_{II} = 2.4\lambda_F$. Comparing with Fig. 23(b), we can observe the corresponding decrease in intermode scattering from mode one to mode three.

Our model of a short quantum point contains a *nonadiabatic*[34] potential. This is completely consistent with the conductance quantization observed in Fig. 12 as long as intermode scattering can occur within these point contacts *without significant backscatter.* Calculations using realistic point contact potentials comprising a single region of constricted width and density appear to confirm these ideas.[35] These same calculations also show that conductance quantization is lost, however, when more than one constricted region is present within the point contact. In this case, backscatter is enhanced by resonance effects, a possibility which becomes greater with increasing point contact length.[32] Furthermore, it has been demonstrated that boundary scattering begins to play a role for lengths $> 0.5$ $\mu$m.[17]

To illustrate that our single-critical-path, *nonadiabatic* model potential preserves conductance quantization, we consider the point contact potential used in case *b* of Fig. 22(a). In Fig. 25, we plot the conductance of the constriction as a function of the saddle-point potential $V_0$. As $V_0$ is increased from 0 to $E_F$, the conductance shows clearly quantized plateaus.

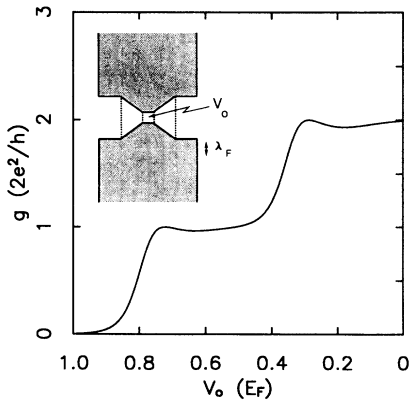


FIG. 25. Nonadiabaticity and conductance quantization. Model potential calculation with $W_I = 1.3\lambda_F$, $L_I = 1.6\lambda_F$, $V_I = V_0$, $L_{II} = 1.6\lambda_F$, $W_{III} = 3.2\lambda_F$, $L_{III} = 1.6\lambda_F$. Conductance plotted as a function of $V_0$ for $V_0$ varied from 0 to $E_F$. At $V_0 = 0.04E_F$, this is the potential used for curve *b* in Fig. 22(a).

### D. Reproducibility of quantum point contact potentials

In the model we have proposed above, we attribute features in the injected flux distribution to details in the potentials of the quantum point contact. In particular, the side lobes of the distribution are expected to be very dependent on intermode scattering, which is, in turn, quite dependent on nonadiabaticity of potentials.

Our method of extracting the transmission coefficients is accomplished by means of a least-squares fit to an overdetermined linear system, as described in Sec. II A. The extra information permits us to study fluctuations in the quantum point contact potential that occur during the four or more hours required to complete the measurement.

We plot the variance in $T_{42}$ in Fig. 26 along with the

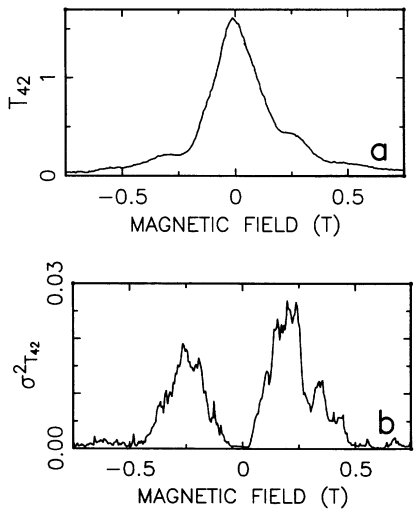


FIG. 26. Variance in $T_{42}$ for the pinched cross junction. (a) $T_{42}$ for bias *c* as determined by the least-squares fit. (b) Corresponding variance $\sigma^2_{T_{42}}$. The variance is peaked at magnetic fields corresponding to those parts of the curve associated with higher-order mode injection.

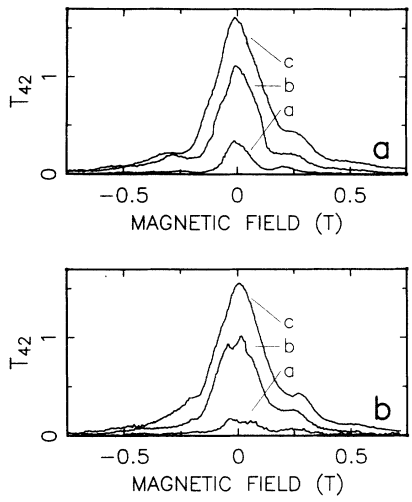


FIG. 27. Reproducibility of point contact potential with thermal cycling. (a) and (b) $T_{42}$ measured on two successive cooldowns. Bias points $a$, $b$, and $c$ are chosen to yield the same quantized ballistic resistance in each case.

least-squares fit $\bar{T}_{42}$ for bias $c$. We note the absolute magnitude of the variance is always $\leq 5\%$. The interesting point to note, however, is that the variance is peaked at magnetic fields corresponding to the shoulders in $T_{42}$, that is, to those parts of the distribution corresponding to higher-order mode injection. It is exactly these features in the curve that we expect to be most sensitive to changes in the point contact potential, since we picture them as arising from the detailed shape of a critical path. Similar peaks in the variance are found for the other transmission coefficients at magnetic fields corresponding to transmission of side-lobe features. We stress that these small changes most likely result from microscopic discrete rearrangement of trapped charge in the $Al_xGa_{1-x}As$, occurring during the course of the several hours required to take the magnetic-field sweeps. During this time, gate bias and temperature are held *fixed.*

In addition, we have studied the reproducibility of point contact potentials with thermal cycling. In Fig. 27, we show $T_{42}$ on two successive cooldowns for a single device. Bias points $a$, $b$, and $c$ are chosen to yield the same quantized ballistic resistance in each case. The potential within the point contact has changed on thermal cycling, although modal features are present in both sets of curves. This variation is also indicative of variations observed from device to device.

### E. Weakly coupled probes

In the case of a ballistic four-probe junction, strong coupling is always obtained when, at the junction, little or no geometrical distinction exists between voltage and current probes. This is exemplified by the *open* cross junction of Fig. 5. There has been considerable theoretical interest in weakly coupled probes as a means of "noninvasively" measuring the voltage drops within small conductors. To realize this opposite extreme requires voltage probes almost totally decoupled from the main current path. Engquist and Anderson[36] define a weakly coupled probe as accepting only infinitesimal transmission $t$ compared to transmission along the main conductor itself, $T$; that is, weak coupling implies $t/T \ll 1$. In our pinched junction, we have achieved weak coupling by using the gated constrictions to separate two of the probes from the main channel.

In Fig. 28, we show the reconstituted Hall resistance for the pinched junction, $R_H(B) = R_{13,24}(B)$. We show the measured value for bias point $c$. (As in the case of the bend resistance measurement, weak-coupling precludes this four-terminal resistance measurement for biases $a$ and $b$.) The quenched Hall effect appears to directly reflect the rebound features observed in turning transmission coefficients. Most surprising is that this effect grows as the probes become decoupled. As we noted previously, with increasing bias, the anomalous rebound peaks acquire similar magnitude to the total flux ultimately collected by the "correct" probe at higher B. Quench of $R_H$ is, thereby *enhanced* by progressive probe decoupling.

Büttiker has applied his four-terminal resistance formalism to consider the special case in which transmission into two of the probes, $t$, is weak.[37] The transmission coefficients for the structure can then be expanded with respect to the small parameter $t$. To lowest order, $T_{31} = T_{31}^{(0)}$, $T_{21} = tT_{21}^{(1)}$, $T_{43} = tT_{43}^{(1)}$. Similar expansions follow for each transmission coefficient. Büttiker then obtains

$$R_{13,24} = \frac{h}{2e^2}\frac{1}{T}\frac{T_{21}^{(1)}T_{43}^{(1)} - T_{23}^{(1)}T_{41}^{(1)}}{(T_{21}^{(1)} + T_{23}^{(1)})(T_{41}^{(1)} + T_{43}^{(1)})}, \tag{27}$$

where $T = T_{31}^{(0)} = T_{13}^{(0)}$. The factor

$$f = \frac{T_{21}^{(1)}T_{43}^{(1)} - T_{23}^{(1)}T_{41}^{(1)}}{(T_{21}^{(1)} + T_{23}^{(1)})(T_{41}^{(1)} + T_{43}^{(1)})} \tag{28}$$

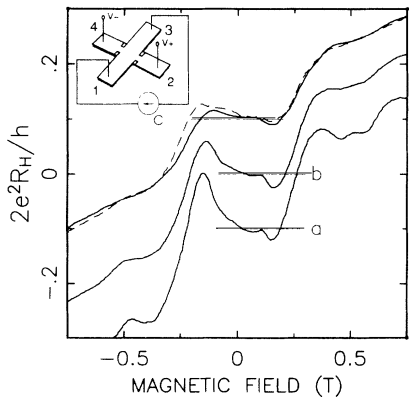


FIG. 28. Hall resistance, $R_H = R_{13,24}(B)$, for the pinched cross junction at biases $a$, $b$, and $c$ reconstituted from the measured $T_{ij}$ (solid curves). Also shown is $R_H$ measured conventionally at bias $c$ (dashed curves). Curves for $a$ and $c$ are offset by 0.1 and −0.1, respectively. Inset: Choice of current and voltage probes for this measurement.

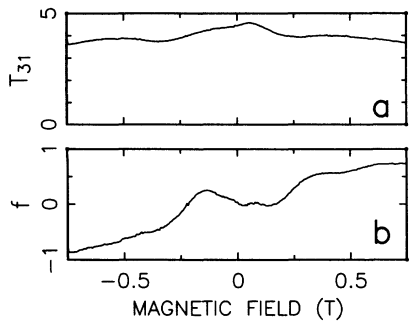


FIG. 29. Form factor [see Eq. (28)] and $T_{31}$ as a function of magnetic field for bias $a$.

is what is identified by Peeters[38] and, later, Akera and Ando[39] as a "geometrical form factor" describing how the Hall resistance vanishes with decreasing magnetic field. This factor clearly depends on the details of the probe coupling.

Using the experimental results of Figs. 16 and 17, we extract the form factor for bias $a$ from Eq. (28). The results are shown in Fig. 29(a). This result differs considerably from previous calculations. All previous theoretical calculations predict form factors which go to zero monotonically as magnetic field goes to zero. These involve simple models in which the weak coupling is achieved by a tunnel barrier in which the transmission is proportional to $|\partial\Psi_0/\partial x|^2$, where $\Psi_0$ is the unperturbed wire wave function and the derivative is evaluated at the wire edge where the voltage probe is attached. However, the form factor we have extracted in Fig. 29 instead shows structure due to the details of the momentum distribution injected by the weakly coupled probes and due to the exact nature of the scattering from the potentials induced in the neighborhood of the probes.

In Fig. 29(b), we also show the transmission coefficient $\tilde{T}_F = T_{31}$ as a function of field. It is relatively constant except for small dips centered at $|B| \sim 0.3$ T. This is probably due to the enhanced backscatter within this field range of certain trajectories from the slight distortions of the main channel in the vicinity of the side probes. In this particular structure, forward collimation alone clearly cannot explain the quenching of $R_H$, contrary to early results of simulations reported by Baranger and Stone.[40]

## V. CONCLUSIONS

We have found that in ballistic semiconductor structures, a single dominant scattering region can be isolated and probed with quasi-one-dimensional leads. An experimental technique is presented for *measuring* the transmission coefficients in specially designed ballistic multiprobe microstructures. It is founded upon theoretical work which treats transport in these structures as a scattering problem.

We measure the scattering properties of a *open* cross junction. There are strong features in the coefficients for turning which can be attributed to simple "rebound" trajectories. These transmission coefficients can be used to successfully calculate any four-terminal resistance.

We also study in detail the *pinched* cross in which two of the probes are separated from the main channel by quantum point contacts. This series arrangement of point contacts allows a sensitive momentum spectroscopy of the emitted distribution, even in the case of nearly vanishing electron flux. Although propagation within the junction is essentially classical in these experiments, transport at the quantum point contact is *not*. In the limit at which only a few modes propagate, we observe side lobes in the emerging beam. This is most evident in the transmission coefficients for propagation through both point contacts. "Rebound" features clearly persist in the turning coefficients for this geometry and show structure due to specular scattering of the side lobes. The side lobes are *modal features* in the outgoing distribution, which are present even in the case of a single propagating mode. We believe that this implies that quantum point contact potentials are, in general, nonadiabatic, even in the presence of conductance quantization. For short contacts, which demonstrate conductance quantization, transport appears to be dominated by a *single* critical path of constricted width and density defined by potential fluctuations produced by the random position of ionized donors. This pinched geometry also allows the first fully characterized realization of weakly coupled probes. We find that signatures of junction scattering persist in this case and are, in fact, *strengthened* in the limit of weak coupling.

## ACKNOWLEDGMENTS

We thank A. Scherer for assistance in fabrication and M. Büttiker for helpful discussions. K.L.S. acknowledges support from the Hertz Foundation and the National Science Foundation through Grant No. EID 87-11693.

## APPENDIX A: SEMICLASSICAL ANALYSIS OF "IMAGING" BY REBOUND TRAJECTORIES

This appendix describes the details of calculating semiclassical propagation of electrons in a magnetic field from an injector to a reflection point a distance $X^+$ away from center.

For $X^+ < X^+_{\rm crit}$, we refer to Fig. 30(a). Introducing the angle $\alpha$, the relevant relations are

$$\tan(\alpha+\theta) = \frac{X^+}{L - 2r_c \sin\theta}, \tag{A1}$$

$$X^{+2} + (L - 2r_c \sin\theta)^2 = 4r_c^2 \sin^2\alpha, \tag{A2}$$

where $r_c = (h/eB)\sqrt{n_s/2\pi}$ is the cyclotron radius. $L$ is the distance between the collector and injector. These relations can be solved to find $\theta(X^+, r_c)$, the angle of emission reflected by the reflection point at $X^+$ at a given

magnetic field. $X^+_{\rm crit}$ is defined such that $\theta(X^+_{\rm crit}, r_c) = 0$.

For $X^+ > X^+_{\rm crit}$, we refer to Fig. 30(b). In this case, the relavant relations are

$$\tan(\alpha + \theta) = \frac{X^+}{L}, \tag{A3}$$

$$X^{+2} + L^2 = 4r_c^2 \sin^2 \alpha \tag{A4}$$

which can be used to find $\theta(X^+, r_c)$.

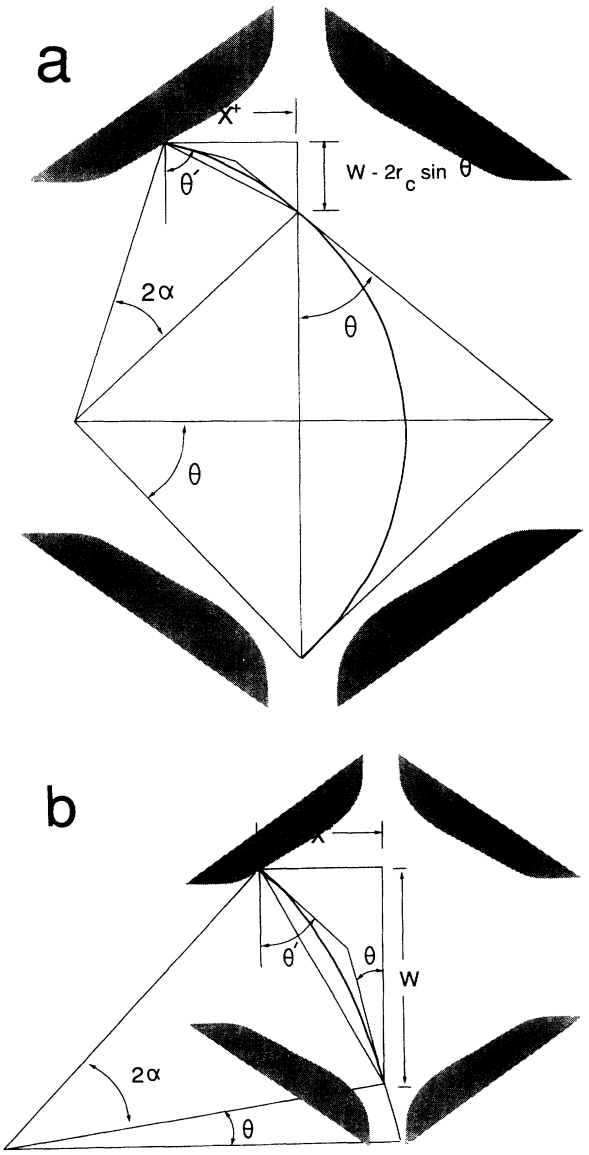


FIG. 30. Classical trajectories for momentum spectroscopy by "rebound." (a) Trajectory for $X^+ < X^+_{\rm crit}$. (b) Trajectory for $X^+ > X^+_{\rm crit}$.

## APPENDIX B: RECURSIVE GREEN'S-FUNCTION CALCULATION OF $dt/d\theta$

In this appendix, we will describe the details of the recursive Green's-function calculations which we have used to calculate the conductance of quantum point contacts and the momentum distributions emitted from such point contacts. The model potential is discretized into lattice points as shown in Fig. 31. Semi-infinite ideal leads 100 lattice constants wide are attached at the left and right to approximate wide 2DEG regions. The free-electron Hamiltonian is similarly discretized into an Anderson tight-binding Hamiltonian.

$$H = \frac{\mathbf{p}^2}{2m} + V(x, y), \tag{B1}$$

$$p_x = -\frac{i\hbar}{2a} \sum_{n,m} [|n, m\rangle\langle n+1, m| - |n+1, m\rangle\langle n, m|], \tag{B2}$$

$$p_y = -\frac{i\hbar}{2a} \sum_{n,m} [|n, m\rangle\langle n, m+1| - |n, m+1\rangle\langle n, m|], \tag{B3}$$

where we have introduced lattice sites indexed by $n$ and $m$. $a$ is the lattice spacing;

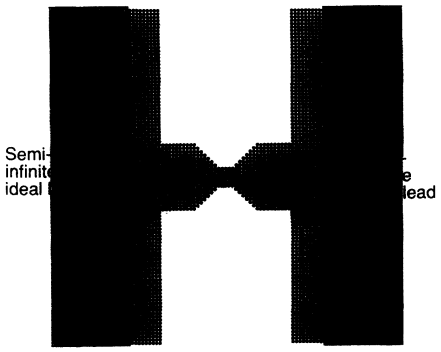


FIG. 31. Discretization of the point contact potential into lattice points for recursive Green's-function calculations. Semi-infinite ideal leads 100 lattice constants wide are attached at the left and right to approximate wide 2DEG regions.

$$H = \sum_{n,m}\{ -\tfrac{1}{2}|n,m\rangle\langle n+1,m| - \tfrac{1}{2}|n+1,m\rangle\langle n,m| + 2|n,m\rangle\langle n,m| \\ -\tfrac{1}{2}|n,m\rangle\langle n,m+1| - \tfrac{1}{2}|n,m+1\rangle\langle n,m| + V_{n,m}|n,m\rangle\langle n,m|\}, \tag{B4}$$

where we have chosen dimensionless units: $[E] = \frac{\hbar^2}{ma^2}$ and $[k] = \frac{1}{a}$.

One now builds up two Green's functions recursively beginning with the Green's function of the semi-infinite ideal lead. Beginning from the left, one calculates the Green's function $\mathbf{G}^L(j)$ in which all columns to the right of $j$ are deleted. The Green's function is a matrix in the subspace of transverse site indices $m$. The relevant recursion relation is

$$\mathbf{G}^L(j) = [\mathbf{G}^0(j)^{-1} - \tfrac{1}{4}\mathbf{G}^L(j-1)]^{-1}, \tag{B5}$$

where $\mathbf{G}^0(j)$ is the Green's function for the isolated $j$ column. Beginning from the right, one similarly builds up the Green's function $\mathbf{G}_R(j)$ in which all columns to the left of $j$ are deleted:

$$\mathbf{G}^R(j) = [\mathbf{G}^0(j)^{-1} - \tfrac{1}{4}\mathbf{G}^R(j+1)]^{-1}. \tag{B6}$$

Two additional relations allow one to build up the Green's functions between any two columns,

$$\mathbf{G}(j,j) = [\mathbf{G}^0(j)^{-1} - \tfrac{1}{4}\mathbf{G}^R(j+1) - \tfrac{1}{4}\mathbf{G}^L(j-1)]^{-1}, \tag{B7}$$

$$\mathbf{G}(j,j'+1) = -\tfrac{1}{2}\mathbf{G}(j,j')\mathbf{G}^R(j'+1). \tag{B8}$$

The Green's functions for the semi-infinite ideal leads are given by

$$\tilde{\mathbf{G}}_L = \tilde{\mathbf{G}}_R = -2\sum_\alpha \chi_\alpha \chi_\alpha^\dagger e^{-ik}, \tag{B9}$$

where the sum is over Fermi-level states with longitudinal wave vector $k > 0$. $\chi_\alpha$ is the transverse lead eigenstate of mode $\alpha$. The energy dispersion is given by

$$E_\alpha(k) = \cos(k) - 1 + \epsilon_\alpha, \tag{B10}$$

where $\epsilon_\alpha$ is the quantized transverse energy of mode $\alpha$.

One computes a matrix $\mathbf{G}(i,i')$, the propagator from column $i$ in lead $i$ to column $i'$ in lead $j$. One can then compute the transmission probabilities from lead $j$ to lead $i$,

$$|t_{ij,mn}|^2 = |\chi_m^{(i)\dagger}\mathbf{G}(i,i')\chi_n^{(j)}|^2 v_m^{(i)} v_n^{(j)}, \tag{B11}$$

where $v_m^{(i)}$ is the velocity of mode $m$ in lead $i$. The conductance can be computed from

$$g = \frac{2e^2}{h}\sum_{mn}|t_{ij,mn}|^2. \tag{B12}$$

We can compute the momentum distribution in the "far-field" limit (many Fermi wavelengths away from the point contact) by noting that in the very wide wires to the right and left of the constriction, the transverse eigenstates are given by

$$\chi_{jn} = \left(\frac{2}{W}\right)^{1/2}\sin(k_y y) = \left(\frac{2}{W}\right)^{1/2}\frac{e^{ik_y y} - e^{-ik_y y}}{2i}, \tag{B13}$$

where $k_y = n\pi/W$, which for $W$ large is a nearly continuous momentum distribution. Deriving an expression for $dT/d\theta$,

$$\frac{dT}{d\theta} = \frac{1}{2\pi}\sum_m |t_{ij,mn}|^2 \left|\frac{dn}{d\theta}\right|, \tag{B14}$$

where we treat $n$ as a continuous variable with

$$n = \frac{k_F W}{\pi}\sin\theta. \tag{B15}$$

Therefore,

$$\frac{dT}{d\theta} = \frac{k_F W}{2\pi^2}\cos\theta\sum_m |t_{ij,mn}|^2. \tag{B16}$$

We use this expression in the calculations of Sec. IV C.

*Present address: IBM Research Division, Thomas J. Watson Research Center, Yorktown Heights, NY 10598.

[1] M. Büttiker, Phys. Rev. Lett. **57**, 1761 (1986).
[2] R. Landauer, IBM J. Res. Dev. **1**, 233 (1957).
[3] R. Landauer, Philos. Mag. **21**, 863 (1970).
[4] R. Landauer, J. Phys. Condens. Matter **1**, 8099 (1989).
[5] Y. Imry, in *Directions in Condensed Matter Physics*, edited by G. Grinstein and G. Mazento (World Scientific, Singapore, 1986), p. 101.
[6] R. Kubo, J. Phys. Soc. Jpn. **12**, 570 (1957).
[7] H. U. Baranger and A. D. Stone, Phys. Rev. B **40**, 8169 (1989).
[8] K. Shepard, Phys. Rev. B **43**, 11 623 (1991).
[9] M. Büttiker, Phys. Rev. B **33**, 3020 (1986).
[10] P. R. Bevington, *Data Reduction and Error Analysis for the Physical Sciences* (McGraw-Hill, New York, 1969), pp. 19 and 59.
[11] H. van Houten *et al.*, Phys. Rev. B **37**, 8534 (1988).
[12] A. Scherer and M. L. Roukes, Appl. Phys. Lett. **55**, 377 (1989).
[13] M. L. Roukes *et al.*, Phys. Rev. Lett. **59**, 732 (1987).
[14] Y. Takagaki *et al.*, Solid State Commun. **68**, 1051 (1988).

[15]G. Timp *et al.*, Phys. Rev. Lett. **60**, 2081 (1988).
[16]M. L. Roukes, A. Scherer, and B. P. van der Gaag, Phys. Rev. Lett. **64**, 1154 (1990).
[17]T. J. Thornton, M. L. Roukes, A. Scherer, and B. P. Van de Gaag, Phys. Rev. Lett. **63**, 2128 (1989).
[18]H. U. Baranger, D. P. DiVincenzo, R. A. Jalabert, and A. D. Stone, Phys. Rev. B **44**, 10 637 (1991).
[19]C. J. B. Ford *et al.*, Phys. Rev. Lett. **62**, 2723 (1989).
[20]M. Büttiker, Phys. Rev. B **41**, 7906 (1990).
[21]L. I. Glazman and M. Jonson, Phys. Rev. B **41**, 10 686 (1990).
[22]K. L. Shepard, M. L. Roukes, and B. P. van der Gaag, Phys. Rev. Lett. **68**, 2660 (1992).
[23]B. J. van Wees *et al.*, Phys. Rev. Lett. **60**, 848 (1988).
[24]D. A. Wharam *et al.*, J. Phys. C **21**, L209 (1988).
[25]C. W. Molenkamp *et al.*, Phys. Rev. B **41**, 1274 (1990).
[26]H. van Houten and C. W. J. Beenakker, in *Nanostructure Physics and Fabrication*, edited by M. Reed and W. P. Kirk (Academic, New York, 1989).
[27]H. van Houten *et al.*, Phys. Rev. B **39**, 8556 (1989).
[28]A. Yacoby and Y. Imry, Phys. Rev. B **41**, 5341 (1990).
[29]This quantity is referred to as simply $T(\theta)$ in Ref. 22.
[30]C. W. J. Beenakker and H. van Houten, Phys. Rev. B **39**, 10 445 (1989).
[31]K. Shepard, Phys. Rev. B **44**, 9088 (1991).
[32]J. A. Nixon, J. H. Davies, and H. U. Baranger, Phys. Rev. B **43**, 12 638 (1991).
[33]A. L. Efros, F. G. Pikus, and G. G. Samsonidze, Phys. Rev. B **41**, 8295 (1990).
[34]E. Castaño and G. Kirczenow, Phys. Rev. B **45**, 1514 (1992).
[35]M. J. Laughton, J. R. Barker, J. A. Nixon, and J. H. Davies, Phys. Rev. B **44**, 1150 (1991).
[36]H.-L. Engquist and P. W. Anderson, Phys. Rev. B **24**, 1151 (1981).
[37]M. Büttiker, IBM J. Res. Dev. **32**, 317 (1988).
[38]F. M. Peeters, Phys. Rev. Lett. **61**, 589 (1988).
[39]H. Akera and T. Ando, Phys. Rev. B **39**, 5508 (1989).
[40]Harold U. Baranger and A. Douglas Stone, Phys. Rev. Lett. **63**, 414 (1989).

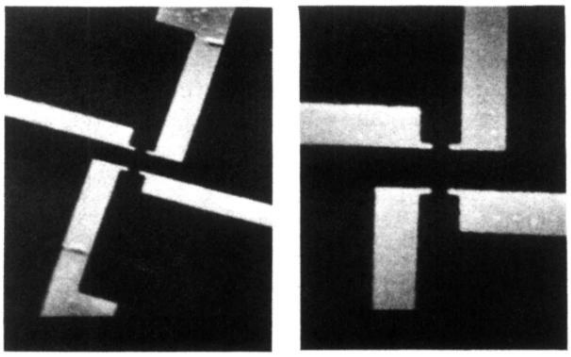

FIG. 11. SEM micrographs of the pinched cross junction. Leads of a cross junction are, as in the case of the open cross junction, defined by gates separated by 400 nm. Here, however, two of these leads are pinched by 150-nm side constrictions formed between two 50-nm-wide gate fingers.

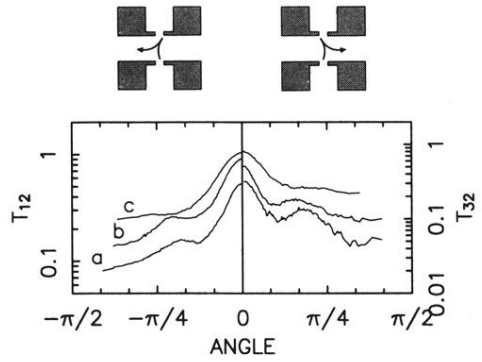


FIG. 18. Imaging with $T_{12}$ and $T_{32}$. "Rebound" portions of $T_{12}$ and $T_{32}$ plotted vs angle of emission. Top: Corresponding simple classical electron trajectories

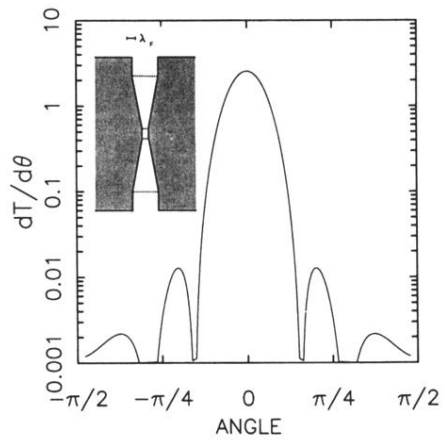


FIG. 19. $dT/d\theta$ for an *adiabatic* constriction with a single propagating mode. The center of the constriction is defined by a potential of height $0.38E_F$ and width $0.95\lambda_F$. The width and potential are graded to $3.2\lambda_F$ and zero, respectively, over a distance of greater than $9\lambda_F$. Inset: Adiabatic point contact potential for the calculation.

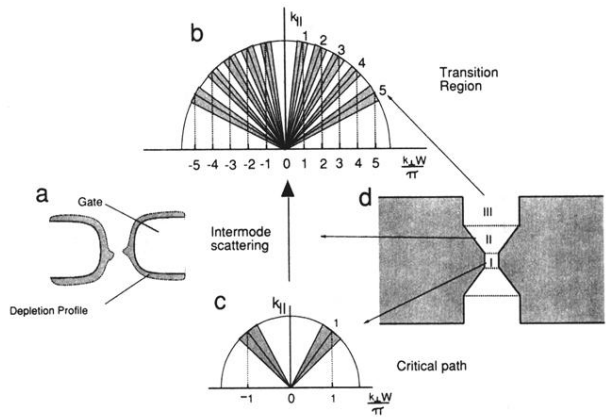


FIG. 21. Critical path model of a quantum point contact. (a) The depletion region defining the *effective* boundaries of the constriction (shaded) do not follow the smooth contour of the gates themselves. (b) Momenta on the $|\mathbf{k}| = k_F$ shell that would be emitted from region III. (c) Momenta on the $|\mathbf{k}| = k_F$ shell that would be emitted from region I. (d) Non-adiabatic model potential. The narrowest region (I) of width $W_{\mathrm{I}}$ and potential $V_{\mathrm{I}}$ empties into the transition region (III) or width $W_{\mathrm{III}}$ and length $L_{\mathrm{III}}$. These are connected by a non-adiabatic region (II), of length $L_{\mathrm{II}}$, with width and potential both linearly graded to match at regions I and III.

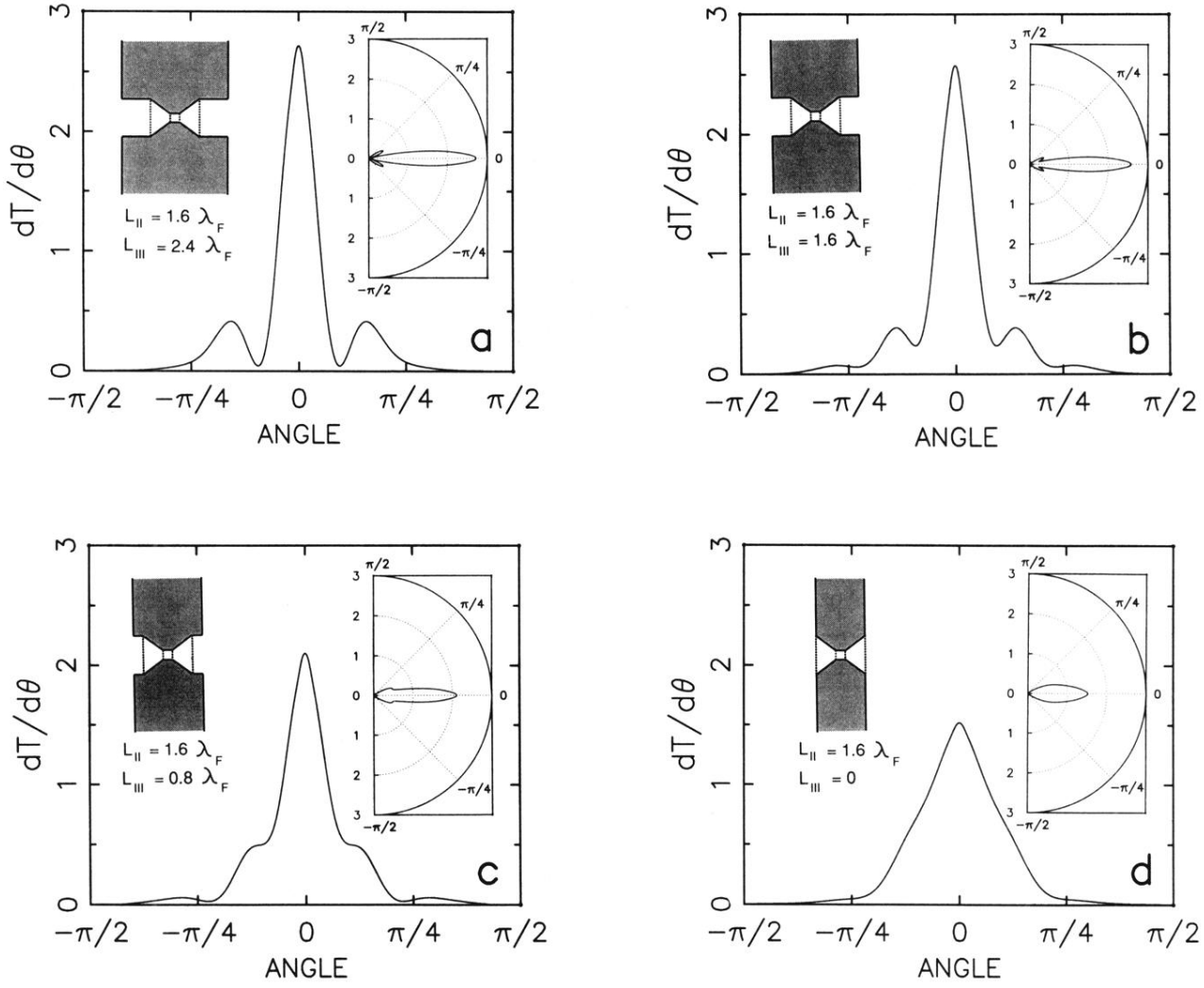


FIG. 23. Importance of the transition region. $dT/d\theta$ for the case of a single mode propagating through the saddle point ($W_{\rm I} = 0.95\lambda_F$, $V_{\rm I} = 0.38E_F$). The nonadiabatic region is of fixed length $L_{\rm II} = 1.6\lambda_F$. Right inset of each plot is a corresponding polar representation. Left inset of each plot is a representation of the model potential. $W_{\rm III}$ is successively reduced. (a) $W_{\rm III} = 2.4\lambda_F$, (b) $W_{\rm III} = 1.6\lambda_F$, (c) $W_{\rm III} = 0.8\lambda_F$, (d) $W_{\rm III} = 0$.

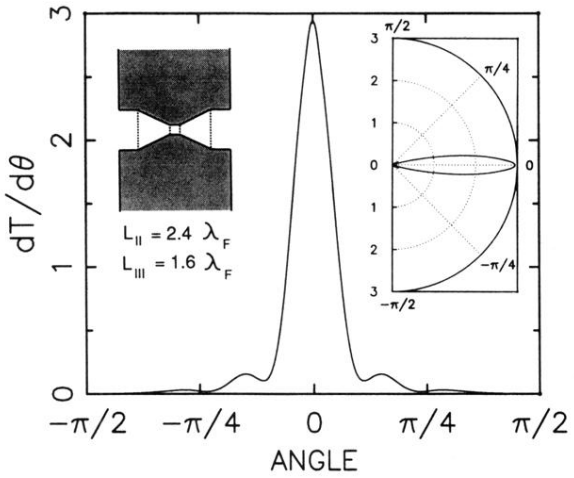


FIG. 24. Importance of the nonadiabatic regon. $dT/d\theta$ for the case of a single mode propagating through the saddle point ($W_{\rm I} = 0.95\lambda_F$, $V_{\rm I} = 0.38E_F$ ) [cf. Fig. 23(b)]. In this case, $L_{\rm II} = 2.4\lambda_F$, $L_{\rm III} = 1.6\lambda_F$. Increasing the length of region II decreases intermode scattering. Right inset: Corresponding polar representation. Left inset: Representation of the model potential.

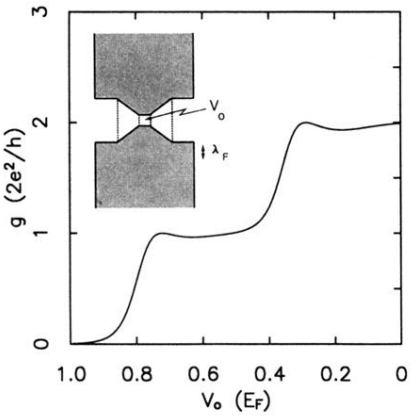


FIG. 25. Nonadiabaticity and conductance quantization. Model potential calculation with $W_{\mathrm{I}} = 1.3\lambda_F$, $L_{\mathrm{I}} = 1.6\lambda_F$, $V_{\mathrm{I}} = V_0$, $L_{\mathrm{II}} = 1.6\lambda_F$, $W_{\mathrm{III}} = 3.2\lambda_F$, $L_{\mathrm{III}} = 1.6\lambda_F$. Conductance plotted as a function of $V_0$ for $V_0$ varied from 0 to $E_F$. At $V_0 = 0.04E_F$, this is the potential used for curve $b$ in Fig. 22(a).

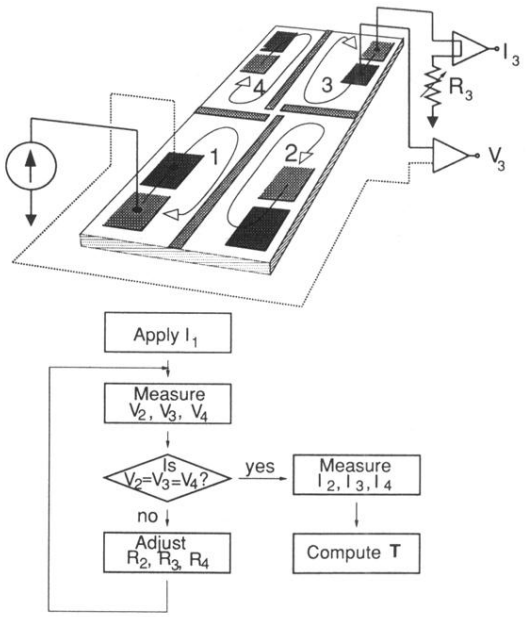


FIG. 3. One possible implementation of the **T**-measurement technique. Arrows show the direction of current flow for $B$ directed upward. Assignment of current (light shading) and voltage (dark shading) contacts depends upon field orientation. For clarity, only connection to reservoirs 1 and 3 are shown.

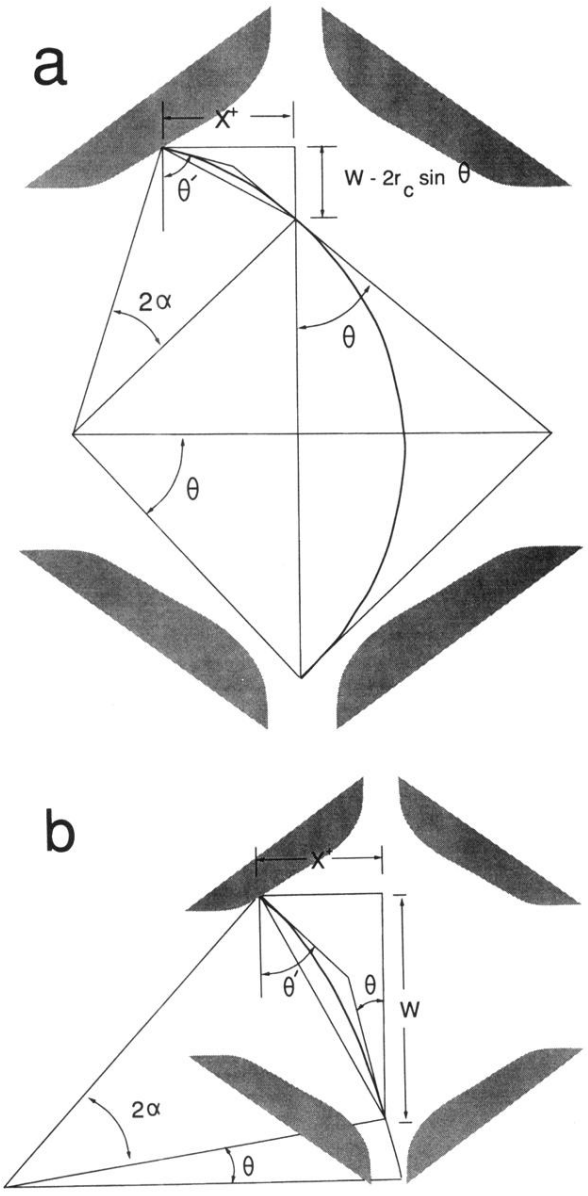


FIG. 30. Classical trajectories for momentum spectroscopy by "rebound." (a) Trajectory for $X^+ < X^+_{\text{crit}}$. (b) Trajectory for $X^+ > X^+_{\text{crit}}$.

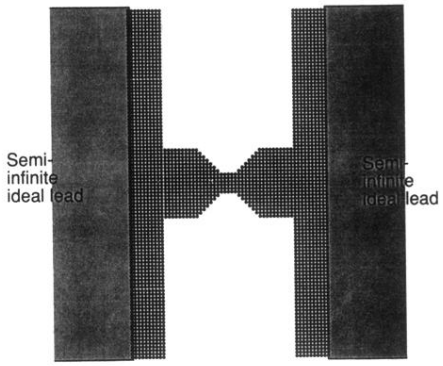


FIG. 31. Discretization of the point contact potential into lattice points for recursive Green's-function calculations. Semi-infinite ideal leads 100 lattice constants wide are attached at the left and right to approximate wide 2DEG regions.

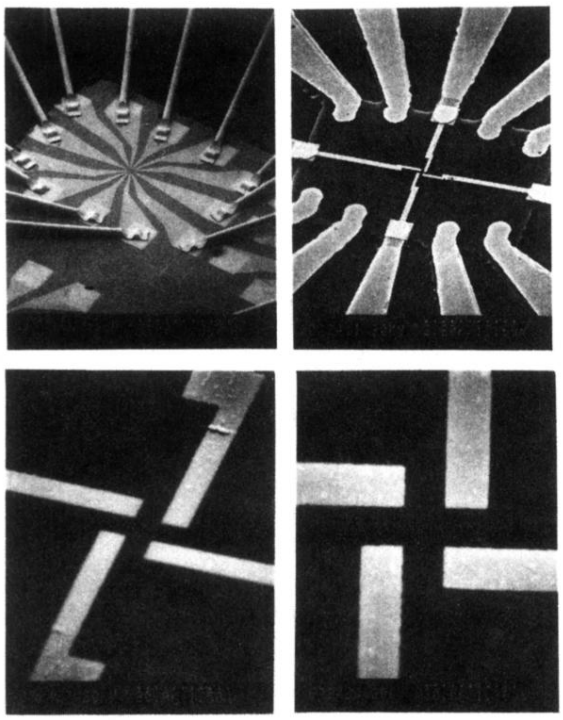

FIG. 5. SEM micrographs of one device used in this study. Top left: Wire bonds attached to twelve Au/Ge Ohmic contacts. Cr/Au fingers lead from these contacts to a central mesa. The devices are $\sim 1$ $\mu$m across. Top right: Central mesa is $20 \times 40$ $\mu$m. Four fingers are isolated from the 2DEG of the mesa by ion exposure. Four Cr-Au gates are then defined. Bottom: These gates form a central cross pattern. Adjacent gates are separated by 400 nm.